communications biology

A Nature Portfolio journal

Article

https://doi.org/10.1038/s42003-025-08153-1

# Coincidence detection between apical and basal dendrites drives STDP in cerebellar Golgi cells



Eleonora Pali[1], Stefano Masoli[1], Danila Di Domenico[1], Teresa Sorbo[1], Francesca Prestori[1,3] & Egidio D'Angelo[1,2,3]

Cerebellar Golgi cells (GoCs), segregate parallel fiber (pf), and mossy fiber (mf) inputs on apical and basal dendrites. Computational modeling predicted that this anatomical arrangement, coupled with a specific ionic channel localization, could be instrumental to drive STDP at mf-GoC synapses. Here, we test this hypothesis with GoC patch-clamp recordings in acute mouse cerebellar slices. Repeated mf-pf pairing on the theta-band within a ± 50 ms time window induces anti-symmetric Hebbian-STDP, with spike-timing long-term potentiation or depression (st-LTP or st-LTD) occurring when action potentials (APs) elicited by pf stimulation follow or precede the activation of mf synapses, respectively. Mf-GoC STDP induction requires AP backpropagation from apical to basal dendrites, NMDA receptor activation at mf-GoC synapses, and intracellular calcium changes. Importantly, STDP is inverted by inhibitory control. Thus, experimental evidence confirms and extends model predictions suggesting that GoC STDP can bind molecular layer to granular layer activity, regulating cerebellar computation and learning.

Several forms of long-term synaptic plasticity have been considered the major cellular substrate for learning and memory in brain circuits[1–3]. In the cerebellum, the concept of synaptic plasticity was initially associated with sensorimotor learning through the motor learning theory, which identified parallel fiber (pf)—Purkinje cell synapses as the plastic site[4,5]. Recently the role of the cerebellum was extended to emotional and cognitive control[6–11]. Moreover, long-term synaptic plasticity was shown to occur in more than 15 different forms both in the granular layer, molecular layer, and deep cerebellar nuclei[12–17]. The mechanisms and role of these forms of plasticity remain largely unsolved in most cases. In the granular layer, which represents the cerebellum input stage, bidirectional long-term synaptic plasticity elicited by patterned mossy fiber (mf) stimulation has been shown in granule cells[18–22] and Golgi cells (GoCs)[23]. GoCs are the main inhibitory interneurons of the granular layer[24–26] and are supposed to exert a significant control over the spatio-temporal transformation of incoming inputs[27–29]. GoCs are interconnected by gap junctions and chemical synapses[30–33], and form both feedforward and feedback inhibitory loops onto granule cells[34]. GoCs receive excitatory inputs from mfs and granule cell ascending axons on the basolateral dendrites and from pfs on the apical dendrites[34,35]. This double input enables GoCs to correlate different cerebellar modules along the pf axis[36,37]. Fundamental issues that remain unexplored are whether and how temporal correlated synaptic inputs impinging onto separate dendritic domains of GoCs could provide the basis for spike-timing dependent plasticity (STDP). Interestingly, NMDA receptors, which are crucial mediators of synaptic plasticity, have been observed at the mf-GoC synapses[35]. Moreover, a variety of voltage-gated $Na^+$, $Ca^{2+}$, and $K^+$ channels, have been found in GoC dendrites[38] and could have a profound impact on dendritic processing. All these aspects have recently been integrated into a realistic computational model of the GoC, which predicted the existence of STDP at mf-GoC synapses under control of action potential (AP) backpropagation from apical to basal dendrites[33]. In this work, using GoC whole-cell patch-clamp recordings in cerebellar slices, we show, for the first time, the existence of anti-symmetric Hebbian STDP at the mf-GoC synapse induced by temporal correlated mf-pf inputs. The induction of this STDP is Hebbian, NMDA receptor-dependent, ms-precise, and related to repeated pairing cycles on the theta-band. Importantly this STDP is fine-tuned by the inhibitory granular layer circuit. These results support the concept that mf-GoC STDP could play a crucial role in regulating information flow through the granular layer under pf control with high temporal precision.

## Methods

All animal manipulations and experimental procedures were approved by the Ethical Committee of the University of Pavia (Italy) and by the Italian Health Office (authorization n. 628/2017-PR and authorization following

[1]Department of Brain and Behavioural Sciences, University of Pavia, Pavia, Italy. [2]Digital Neuroscience Centre, IRCCS Mondino Foundation, Pavia, Italy. [3]These authors jointly supervised this work: Francesca Prestori, Egidio D'Angelo. e-mail: francesca.prestori@unipv.it; dangelo@unipv.it

art. 1, comma 4 of the D. Lgs. N. 26/2014 approved on 09/09/2022) in accordance with the international guidelines of the European Union Directive 2010/63/EU.

### Animals

Animals were grouped-housed on a 12 h light/dark cycle with constantly monitored temperature and humidity, and free access to food and water. Experiments were performed on 16- to 21-day-old (P0 = day of birth) GlyT2-eGFP mice (of either sex) heterozygous for the bacterial artificial chromosome insertion of eGFP under the control of the glycine transporter type 2 gene[39]. GlyT2-eGFP mice were bred on the C57BL/6 genetic background and maintained as heterozygotes.

### Slices preparation and maintenance

GlyT2-eGFP mice were sacrificed by rapid decapitation under deep anesthesia with halothane (Sigma-Aldrich) to isolate the cerebellum using a well-established procedure[35,40]. The dissected cerebellum was then fixed on the vibroslicer's stage (Leica VT1200S; Leica Biosystems) with cyano-acrylic glue and acute slices (220 µm) were cut in the coronal plane in ice-cold (2–3 °C) cutting-solution containing the following (in mM): potassium gluconate 130, KCl 15, ethylene glycol-bis (β-aminoethyl ether) N,N,N',N'-tetraacetic acid (EGTA) 0.2, *N*-2-hydroxyethyl piperazine-*N*-2-ethanesulphonic acid (Hepes) 20, glucose 10, pH 7.4 with NaOH[41]. After cutting, slices were immediately transferred into oxygenated bicarbonate-buffered (Krebs) solution, containing the following (in mM): NaCl 120, KCl 2, $MgSO_4$ 1.2, $NaHCO_3$ 26, $KH_2PO_4$ 1.2, $CaCl_2$ 2, glucose 11 (pH 7.4 when equilibrated with 95% $O_2$–5% $CO_2$) and incubated in a submerged chamber at 32 °C for at least 1 h. In the recording chamber mounted on the stage of an upright microscope (Olympus), slices were continuously perfused with oxygenated Krebs' solution (1.5 ml/min) maintained at 32 °C through a Peltier feedback device (TC-324B, Warner Instrument Corp.).

### Pharmacology

Unless stated otherwise, inhibitory synaptic transmission was continuously blocked by bath-applying 1 µM strychnine hydrochloride (strychnine; Sigma-Aldrich) and 10 µM SR 95531 (6-imino-3-(4-methoxyphenyl)-1(6H)-pyridazinebutanoic acid hydrobromide, gabazine; Abcam), a glycinergic receptor antagonist and $GABA_A$ receptor antagonist, respectively. In some experiments, 100 µM D-2-amino-5-phosphonovalerate (D-APV; Abcam) and 50 µM 7-chlorokynurenic acid sodium salt (7-Cl Kyn; Abcam) were added to the Krebs' solution to block NMDA receptors. All drugs were prepared in water and stored at −20 °C, then diluted (1:1000) in external bath solution when being used.

### Whole-cell recordings

Slices were visualized under an upright epifluorescence microscope (Olympus) equipped with a 40× (numerical aperture NA = 0.8) water-immersion objective (Olympus). Whole-cell patch-clamp recordings were performed from the soma of visually identified GoCs in lobules VII and VIII. Patch pipettes (3–5 MΩ) were produced from standard borosilicate glass capillaries (Sutter Instruments) using a Sutter P-1000 horizontal puller (Sutter Instrument) and filled with an intracellular solution containing the following (in mM): potassium gluconate 145, KCl 5, HEPES 10, EGTA 0.2, $MgCl_2$ 4.6, ATP-$Na_2$ 4, and GTP-$Na_2$ 0.4, adjusted at pH 7.3 with KOH. Whole-cell patch-clamp recordings were obtained using a Multiclamp 700B amplifier and pClamp data acquisition software and were sampled at 50 kHz using a Digidata 1440 A interface (Molecular Devices, USA). In a different series of recordings, EGTA was increased to 10 mM. Signals were analyzed off-line with pClamp10.7 software (Molecular Devices, USA). Excitatory post-synaptic currents (EPSCs) were low-pass filtered at $f_c$ = 10 kHz (−3 dB). Recordings were discarded when the basal current measured at −70 mV was negative to −150 pA, consistent with previous works[23,40]. Series resistance ($R_s$) was constantly monitored throughout the recording (3.4 ± 0.1 MΩ, $n$ = 151) and compensated by 10–60%. Only recordings with stable $R_s$ were accepted (changes < 20%). The liquid junction potential between the bath and pipette solutions was measured according to[42] and was 10 mV. Membrane potential values were stated without adjustment for liquid junction potentials.

### Golgi cell identification

Fluorescent GoCs, which represent 86% of the entire GoC population, were visually identified[41,43,44]. It should be noted that other glycinergic interneurons of the granular layer also exhibit GFP-positivity, specifically Lugaro cells and globular cells[39,43]. To distinguish GoCs from Lugaro cells (globular cells are considered a subtype of Lugaro cells[32,45,46], a combination of morphological and electrophysiological criteria was used: (1) we targeted GFP-positive neurons located in the middle of the granular layer (see Supplementary Fig. 1B), as Lugaro cells are typically positioned just beneath Purkinje cells[34,47]; (2) we selected neurons with rounded and large (>15 µm diameter) soma (see Supplementary Fig. 1B), since Lugaro cells have smaller soma and exhibit an elongated shape; (3) recorded neurons revealed the typical membrane capacitance ($C_m$ = 49.4 ± 1.1 pF, $n$ = 151) and input resistance ($R_{in}$ = 127.9 ± 4.9 MΩ, $n$ = 151) of GoCs, which are characterized by the largest soma, axonal plexus, and dendritic tree among granular layer neurons[23,40,48]; (4) recorded neurons showed spontaneous firing (6.2 ± 0.9 Hz, $n$ = 32, $N$ = 27) and sagging inward rectification in response to hyperpolarizing current steps (see Supplementary Fig. 1C), typical of GoCs[43]. Finally, several neurons were filled with 50 µM Alexa Fluor 594 and morphologically identified revealing the typical GoC morphology (see Supplementary Fig. 1B).

### Stimulation

Mfs and pfs were stimulated using two glass monopolar electrodes (1–2 MΩ, 3–10 µm diameter) filled with Krebs' solution and positioned in the white matter and molecular layer, respectively (see Supplementary Fig. 1A).

EPSCs were evoked at −70 mV before and after inducing STDP, stimulating for either ten (control condition) or 30 min (post- STDP induction condition) the mf bundle with 200 µs-square voltage steps applied at 0.1 Hz (test frequency) using a stimulus isolator system. Based on previous works[35,49], GoC evoked EPSCs can show either a short latency response (one peak per stimulus) or a mix of short- and long-latency responses (multiple peaks per stimulus). Indeed, a pipette positioned in the mf bundle, not only activates GoC basal dendrites through a monosynaptic pathway (mf → GoC) but also granule cell dendrites inside the glomerulus. Granule cell dendrites, in turn, make synaptic contacts with GoC apical dendrites via their axonal projections, thereby generating a disynaptic pathway (mf → granule cell → GoC). Here, 76 out of 151 recorded GoCs show purely short-latency responses (time to peak = 1.8 ± 0.03 ms), while 75 out of 151 show a mix of short- and long-latency responses (59 out of 75: time to second peak = 4.2 ± 0.08 ms; 16 out of 75: time to third peak = 6.5 ± 0.5 ms). Interestingly, a higher occurrence of purely short-latency responses was observed in the coronal plane (50.3%) compared to our previous work (17.6%) conducted in the sagittal orientation[23]. This could potentially be attributed to the observation that GoC apical dendrites appear to be constrained within a specific cerebellar stripe in the coronal plane[50], in contrast to the sagittal plane, where they extend longitudinally for up to 300 µm[35].

In a set of experiments, to evaluate the mechanism of STDP expression, EPSCs were evoked through paired-pulse stimulation of the mf bundle. Precisely, two stimuli were delivered 20 ms apart and repeated every 5 s (0.2 Hz) for either 10 min (control condition) or 30 min (post-STDP induction condition).

### STDP induction protocol

STDP was induced from a holding potential ($V_{hold}$) of about −60 mV by pairing mf–pf stimulations 60 times at 1, 4, 6, or 10 Hz with a fixed time difference (Δt = ±10, ±25, ±50 or ±100 ms; see Supplementary Table 1). Δt was defined as the time difference between the onset of the mf-EPSP (excitatory postsynaptic potential evoked stimulating mfs) and the peak of the pf-AP (action potential evoked stimulating pfs). According to canonical

pair-based STDP rules, a negative spike-timing interval was considered when mf-EPSP arrived after pf-AP (pf-AP → mf-EPSP), while a positive spike-timing interval was considered when mf-EPSP arrived before pf-AP (mf-EPSP → pf-AP).

To determine whether STDP depends on the APs elicited by pf stimulation, three distinct sets of experiments were conducted in which pf activation was replaced by alternative conditions. First, the pf stimulus was replaced with a mf stimulus to induce STDP while selectively activating basal dendrites. To ensure appropriate pairing during STDP induction, two spatially distinct stimuli were applied to the mfs: one designed to elicit APs (mf-AP) and the other to evoke only EPSP (mf-EPSP). Second, somatic AP generation was mimicked by injecting a depolarizing current into the soma of GoCs either before or after mf stimulation (GoC-AP → mf-EPSP or mf-EPSP → GoC-AP). Lastly, a subthreshold pf stimulation was delivered both before and after mf activation (pf-EPSC → mf-EPSP or mf-EPSP → pf-EPSC).

### EPSC analysis

All EPSCs were digitally filtered at 1.5 kHz and analyzed off-line using pClamp10.7 (Molecular devices, USA). Consistent with previous works[23,35], short-latency responses were considered when the time to peak was minor to 2.0 ms. EPSC amplitude was measured as the difference between EPSC peak and the current level just before stimulation. Long-term synaptic efficacy changes (percent change, %change) were measured after 30 min. A 10 min period was used to evaluate mean EPSC amplitude (control condition). Data are reported as mean ± SEM ($n$ = X cells, $N$ = $Y$ animals).

### Statistics and reproducibility

Data normality was assessed using the Shapiro–Wilk test. Statistical significance was determined using either a Student's $t$ test or one-way ANOVA, followed by Tukey's post hoc test where appropriate. All analyses were two-sided, with a significance level of $\alpha = 0.05$.

For each experimental series, a retrospective power and sample size (PSS) analysis was performed with a power of 0.9, confirming that the reported sample size was adequate to accurately detect the effects of interest. All statistical analyses were conducted using OriginPro 8.

### PPR and CV analysis

To investigate the expression mechanism of STDP, the analysis of both paired-pulse ratio (PPR) and coefficient of variation (CV) was performed by measuring the mean and standard deviation (SD) of EPSC amplitude[21,51]. All measurements were performed over $n = 60$ contiguous EPSCs minimizing errors introduced by small samples. The PPR was measured as the ratio of the amplitude of the second EPSC ($EPSC_2$) to the amplitude of the first EPSC ($EPSC_1$) in a pair of stimuli, $PPR = EPSC_2/EPSC_1$, whereas the CV of EPSCs was measured as SD divided by the mean amplitude of EPSCS (M), CV = SD/M.

### Post hoc visualization of Alexa Fluor 594-filled Golgi cells

In some experiments, recorded GoCs were filled with 50 µM Alexa Fluor 594 and identified by immunocytochemistry. After recording, the cerebellar slices were fixed in PBS containing 4% paraformaldehyde for 30 min and then washed for at least 20 min with PBS. The slices were then stained with DAPI (ref. R37606, Invitrogen) and mounted in Fluoromount-G (ref 00–4958, Invitrogen). Images were captured using Leica TCS SP8 STED 3X confocal microscope (Centro Grandi Strumenti, University of Pavia). Z-stack images were acquired for Golgi cell visualization and morphological reconstruction and then analyzed with the LASX software.

### Golgi multicompartmental model

A multi-compartmental GoC model was built to reproduce intrinsic and synaptic responses[46] and was extended with a plasticity mechanism based on calcium dynamics[52] that was parameterized as reported previously[53]. GoCs have active basal and apical dendrites that express $Ca^{2+}$, $Na^{+}$, and $K^{+}$ channels. To isolate calcium entry specifically generated by NMDA receptors, these receptors were confined to "spine-like" micro-domains measuring 2.5 µm length and 0.58 µm width. The dimension of this "spine-like" structure was estimated based on the average dimensions of the terminal dendrites in the model morphology. Except for AMPA and NMDA receptors and leakage channels, no other ionic channels are present in these micro-domains. The AMPA receptor was modified to exhibit the same paired-pulse facilitation observed at mf-GoC synapses. Additionally, calcium pump kinetics were accelerated fourfold compared to the control condition to modulate calcium concentration in the micro-domain. Shouval-Bear equations (see Supplementary Material) generated a value (ranging from 0 to 1) based on the micro-domain calcium concentration. This value was then used to modify the current generated by AMPA receptors located on basal dendrites[52].

$$G_{AMPA} = g_{max} + (400\,pS * (2 * (w - 1)) * Q10 * O$$

The parameters used in the equations are as follows: $G_{AMPA}$ is the AMPA conductance, with $g_{max}$ representing the initial conductance of 1200 pS; $w$ is the value calculated using Shouval-Bear equations (see Supplementary Material), $Q10$ is the temperature coefficient, and $O$ denotes the open state. The same equation was also applied to the NMDA receptor.

The Shouval–Bear equations were originally tested with fixed calcium concentration, so the value of $w$ cannot be maintained during the induction of either LTD or LTP. As $w$ fluctuates in response to changes in calcium concentration, and since the difference in calcium levels between LTD and LTP is minimal, a threshold was introduced below which $w$ remains at the LTD level. If the calcium concentration exceeds this threshold, an increased calcium flow is triggered through the NMDA channel. This approach accounts for calcium-induced calcium release from intracellular stores, which are not explicitly modeled.

Simulations were performed with 30 pf synapses randomly distributed on the apical dendrites and 20 mf synapses randomly distributed on the basal dendrites. The induction protocol was like the experimental one: mf-pf pairing was performed in current-clamp mode with a Δt of ±25 ms, and the stimulations were repeated 60 times at 4 Hz. EPSCs were recorded in voltage-clamp at −70 mV, with six synaptic stimuli delivered at 0.3 Hz before and after the induction protocol. Additionally, according to our experimental results, a PPR value of 1.5 was incorporated into the model. The model was written in Python 3 and NEURON 8[54]. Calcium concentration, AMPA and NMDA currents, and the value of $w$ were recorded in HDF5 files, which were later analyzed using a custom Python script.

### Reporting summary

Further information on research design is available in the Nature Portfolio Reporting Summary linked to this article.

## Results

Whole-cell patch-clamp recordings were performed from Golgi cells in acute cerebellar slices of juvenile GlyT2-eGFP mice (P16-P21) using stimulation protocols designed to determine the presence of STDP.

### STDP at mossy fiber-Golgi cell synapses is governed by phase differences between mossy and parallel fiber inputs

Following the prediction of a detailed GoC model[33], electrophysiological recordings were designed to deliver pf-AP → mf-EPSP or mf-EPSP → pf-AP pairings repeated 60 times at 4 Hz using Δt = ±10, ± 25, ±50 or ±100 ms (Fig. 1). pf-AP → mf-EPSP pairing at Δt = −10 and −25 ms induced significant st-LTD (Δt = −10 ms: −34.2 ± 11.4%, $n = 6$, $N = 4$, Student's paired $t$ test, $p = 0.049$; Δt = −25 ms: −33.6 ± 4.7%, $n = 6$, $N = 5$, Student's paired $t$ test, $p = 0.006$; Fig. 1A, B), while mf-EPSP → pf–AP pairing at Δt = +10 and +25 ms induced significant st-LTP (Δt = +10 ms: 25.4 ± 5.3%, $n = 6$, $N = 4$, Student's paired $t$ test $p = 0.03$; Δt = +25 ms: 27.1 ± 7.5%, $n = 6$, $N = 6$, Student's paired $t$ test, $p = 0.01$; Fig. 1A, B). In all cases, st-LTD and st-LTP persisted nearly unchanged for the entire duration

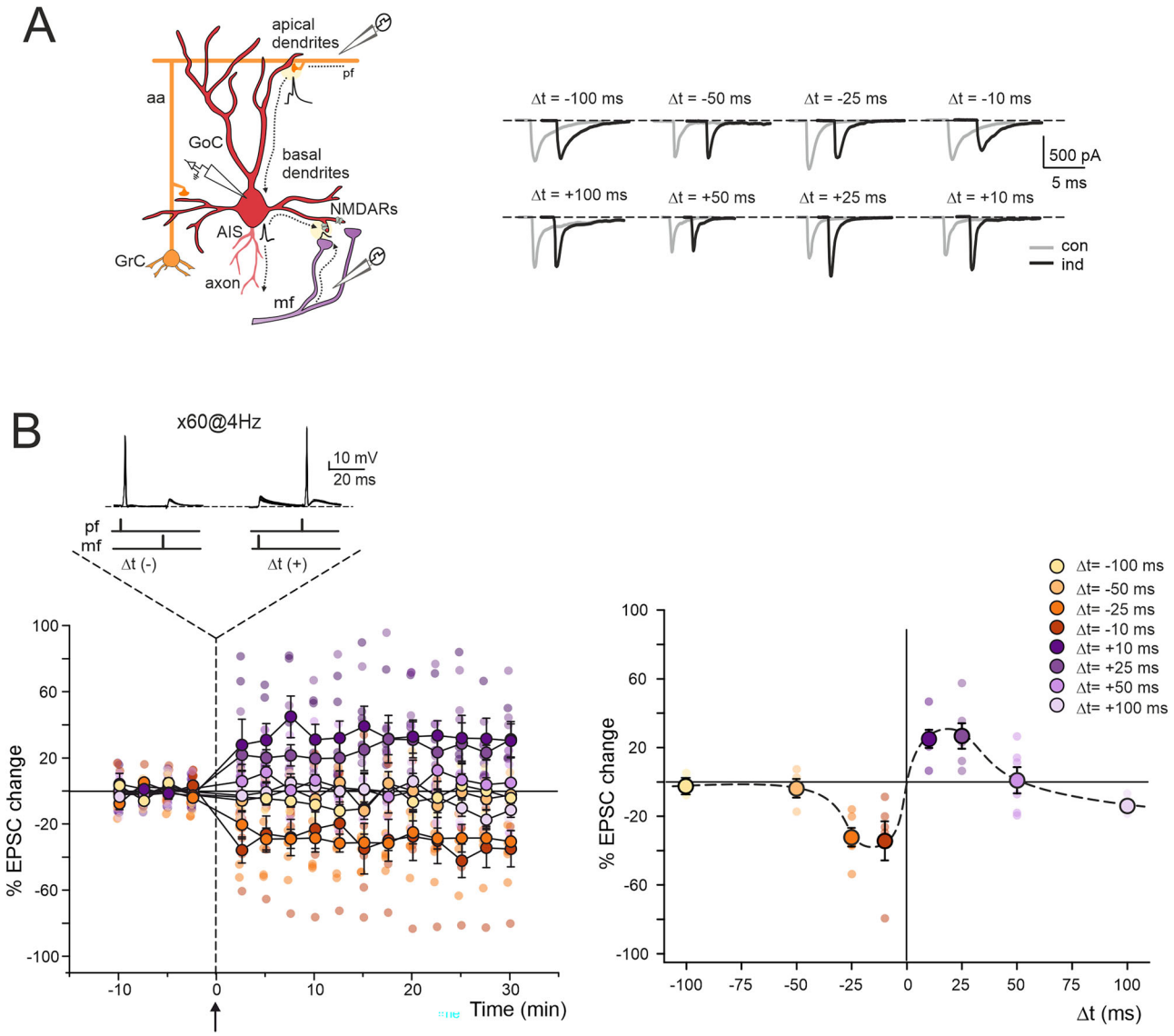


**Fig. 1 | Experimental evidence of STDP at the mf-GoC synapse. A** Left, enlargement of the GoC microcircuit, illustrating the afferent excitatory inputs from pfs/aas and mfs onto apical and basal dendrites, respectively, and the process of dendritic integration revealed by the previous modeling work[33]. The illustration has been created with CorelDRAW 2019. Right, EPSCs (average of 30 individual sweeps) evoked by mf stimulation before (*con*-, gray traces) and 30 min after (*ind*-, black traces) STDP induction, with different pairing time windows (Δt = ±10, ± 25, ±50 or ±100 ms). **B** Left, plot shows the time course of EPSC amplitude changes (expressed as the percent change of EPSC amplitude with respect to baseline) for each Δt. The plot shows the time course of average EPSC changes (large dots), with individual recordings overlaid (small dots) per Δt (Δt = −10 ms: $n = 6$, $N = 4$, $p = 0.049$; Δt = −25 ms: $n = 6$, $N = 5$,; Δt = +10 ms: $n = 6$, $N = 4$, $p = 0.03$; Δt = +25 ms:, $n = 6$, $N = 6$, $p = 0.01$; Δt = −50 ms:, $n = 4$, $N = 4$, $p = 0.34$; Δt = −100 ms: $n = 3$, $N = 3$, $p = 0.44$; Δt = +50 ms: $n = 6$, $N = 6$, $p = 0.92$; Δt = +100 ms:, $n = 3$, $N = 3$, $p = 0.13$; mean ± SEM; Student's paired *t* test; some standard errors are small and fall inside the dots). The arrow indicates the STDP induction time (pf-AP → mf-EPSP or mf-EPSP → pf-AP pairing, 60 times at 4 Hz). Right, STDP timing curve showing EPSC amplitude changes in individual recordings 30 min after induction (small dots), and average EPSC changes (large dots). Bars indicate mean ± SEM (some standard errors are small and fall inside the dots). Note that mf-GoC STDP is Hebbian and anti-symmetric.

of recordings (Fig. 1A, B). Therefore, consistent with anti-symmetric Hebbian STDP[55–60], this plasticity at mf-GoC synapses is anti-symmetric and order-dependent. This STDP also shows precise time windows for st-LTP and st-LTD. In fact, either st-LTD or st-LTP vanished with Δt ≥ ±50 ms (Δt = −50 ms: −3.5 ± 5.4%, $n = 4$, $N = 4$, Student's paired *t* test, $p = 0.34$; Δt = −100 ms: −2.2 ± 3.9%, $n = 3$, $N = 3$, Student's paired *t* test, $p = 0.44$; Δt = +50 ms: 1.3 ± 7.7%, $n = 6$, $N = 6$, Student's paired *t* test, $p = 0.92$; Δt = +100 ms: −13.7 ± 3.5%, $n = 3$, $N = 3$, Student's paired *t* test, $p = 0.13$; Fig. 1A,B). The phase-plot shows similar but opposite changes in EPSC amplitude for each ± Δt pairing uncovering the anti-symmetric nature of mf-GoC STDP (Fig. 1B)[61–64]. Unless otherwise indicated, the data reported below refer to st-LTP at Δt = +25 ms and st-LTD at Δt = −25 (i.e., where the STDP changes were the largest). Collectively, the temporal order and the phase difference between mf and pf inputs emerged as the two critical determinants governing the sign and magnitude of mf-GoC plasticity configuring a form of anti-symmetric Hebbian STDP.

The GoC model[33] was implemented using the Shouval-Bear equations[52] to simulate STDP pairing pf-EPSP → mf-EPSP or mf-EPSP → pf-EPSP with Δt = ± 25 ms repeated 60 times at 4 Hz. These simulations showed that pf-AP → mf-EPSP induced st-LTD (−16.9 ± 4.1%, $n = 20$ synapses, Student's paired *t* test $p = 0.007$), while mf-EPSP → pf-AP induced st-LTP (15.8 ± 4.4%, $n = 20$ synapses, Student's paired *t* test $p = 6 \times 10^{-5}$) confirming that mf-GoC synapses indeed support STDP (Fig. 2A, B).

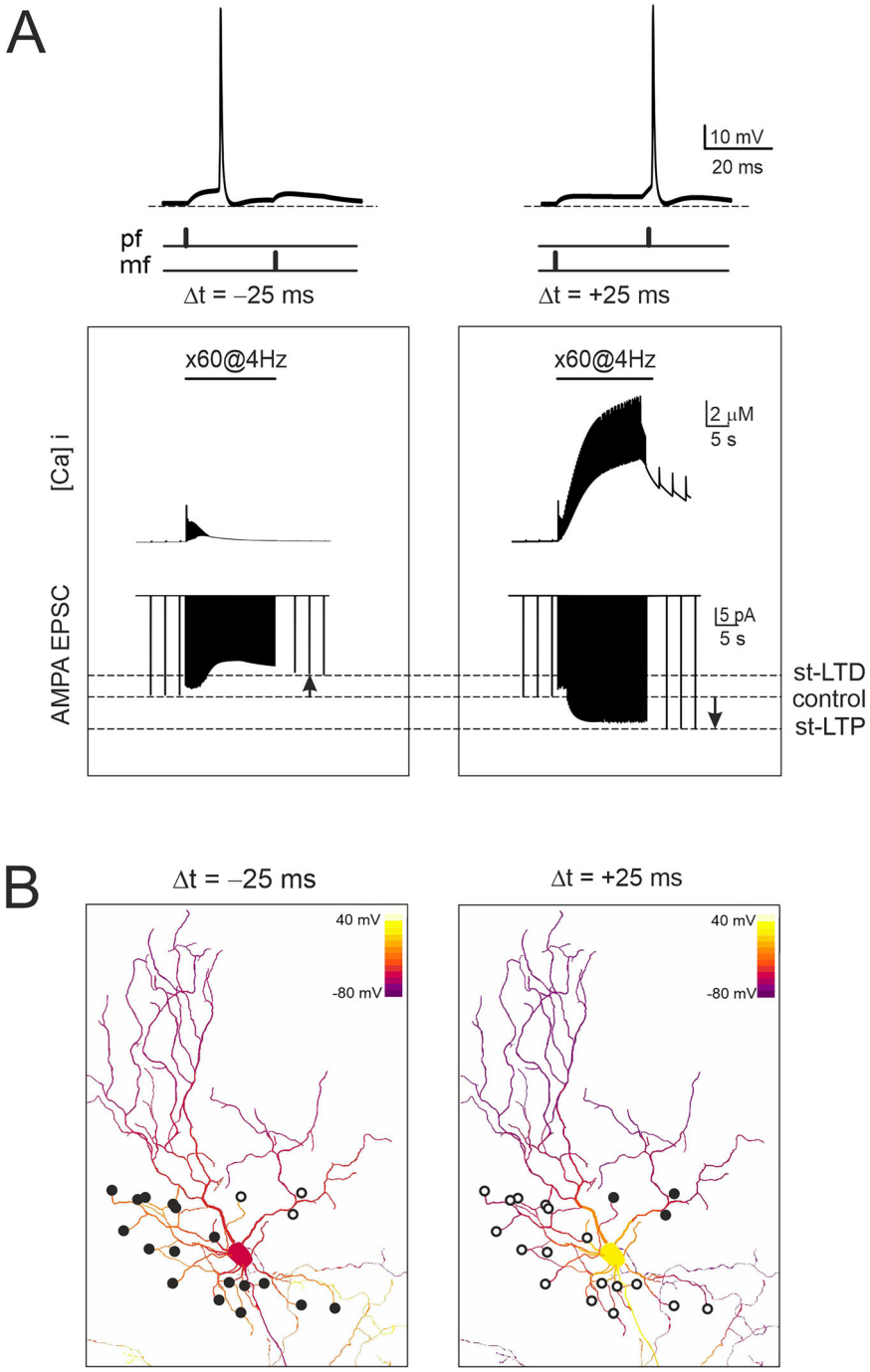


**Fig. 2 | Model simulations of STDP at the mf-GoC synapse. A** Model simulations of STDP. Top traces show membrane potential changes recorded from the GoC soma during pf-AP → mf-EPSP and mf-EPSP → pf-AP pairings (Δt = −25 ms: $n = 20$ synapses, $p = 0.007$; Δt = + 25 ms: $n = 20$ synapses, $p = 6 \times 10^{-5}$; Student's paired *t*test). The lower panels show the AMPA EPSCs and $[Ca^{2+}]_i$ changes caused by the NMDA current in basal dendrite during STDP induction (60 times at 4 Hz). **B** Simulated GoC membrane potential changes during STDP induction shown in false colors (bottom scale is −80 mV, top scale +40 mV). The two pictures show model simulations with pf-AP → mf-EPSP and mf-EPSP → pf-AP pairing at Δt = ± 25 ms. The STDP expression is indicated for all the synapses activated in the simulation (filled circles, st-LTP; open circles st-LTD).

## STDP requires the action potential elicited by parallel fiber stimulation

The backpropagation of APs from axonal initial segment (AIS) to dendrites generates the associative signal critical for inducing modifications at active synapses[56,65,66]. Based on our GoC model[33], synaptic activation of GoC apical dendrites by pfs can trigger AP generation at the AIS, followed by a rapid backpropagation into basal dendrites, providing the associative signal for STDP induction. To test this hypothesis, we performed three different sets of experiments (Fig. 3).

First, we replaced the pf stimulus with a mf stimulus to induce STDP thereby activating only basal dendrites (Fig. 3A). We applied two spatially distinct stimuli to the mfs: one to elicit APs and the other to evoke only EPSPs, providing the pairing needed for STDP induction. Both mf-AP → mf-EPSP and mf-EPSP → mf-AP pairing induced LTD (mf-AP → mf-EPSP: −24.3 ± 5.1%, $n = 5$, $N = 4$, Student's paired $t$ test $p = 0.03$; mf-EPSP → mf-AP: −23.9 ± 7.4%, $n = 5$, $N = 5$, Student's paired $t$ test $p = 0.03$). These results indicate that activating basal dendrites alone is insufficient to induce anti-symmetric Hebbian STDP, suggesting distinct roles for apical and basal inputs in GoC synaptic integration, likely driven by the differential expression of $Ca^{2+}$ channels and $Ca^{2+}$-dependent $K^+$ channels across the two dendritic compartments[30,33,38] (see also Supplementary Fig. 2).

Moreover, we mimicked the depolarization caused by the AP by injecting a positive current into the soma of GoCs, either before or after mf stimulation (Fig. 3B). Surprisingly, both GoC-AP → mf-EPSP and mf-EPSP → GoC-AP pairing failed to induce STDP (GoC-AP → mf-EPSP: 4.8 ± 4.2%, $n = 5$, $N = 4$, Student's paired $t$ test $p = 0.29$; mf-EPSP → GoC-AP: −4.5 ± 7.7%, $n = 5$, $N = 5$, Student's paired $t$ test $p = 0.69$). These findings confirm that STDP is not solely dependent on the temporal correlation of AP-EPSP pairing but also on the specific GoC compartment where APs are generated.

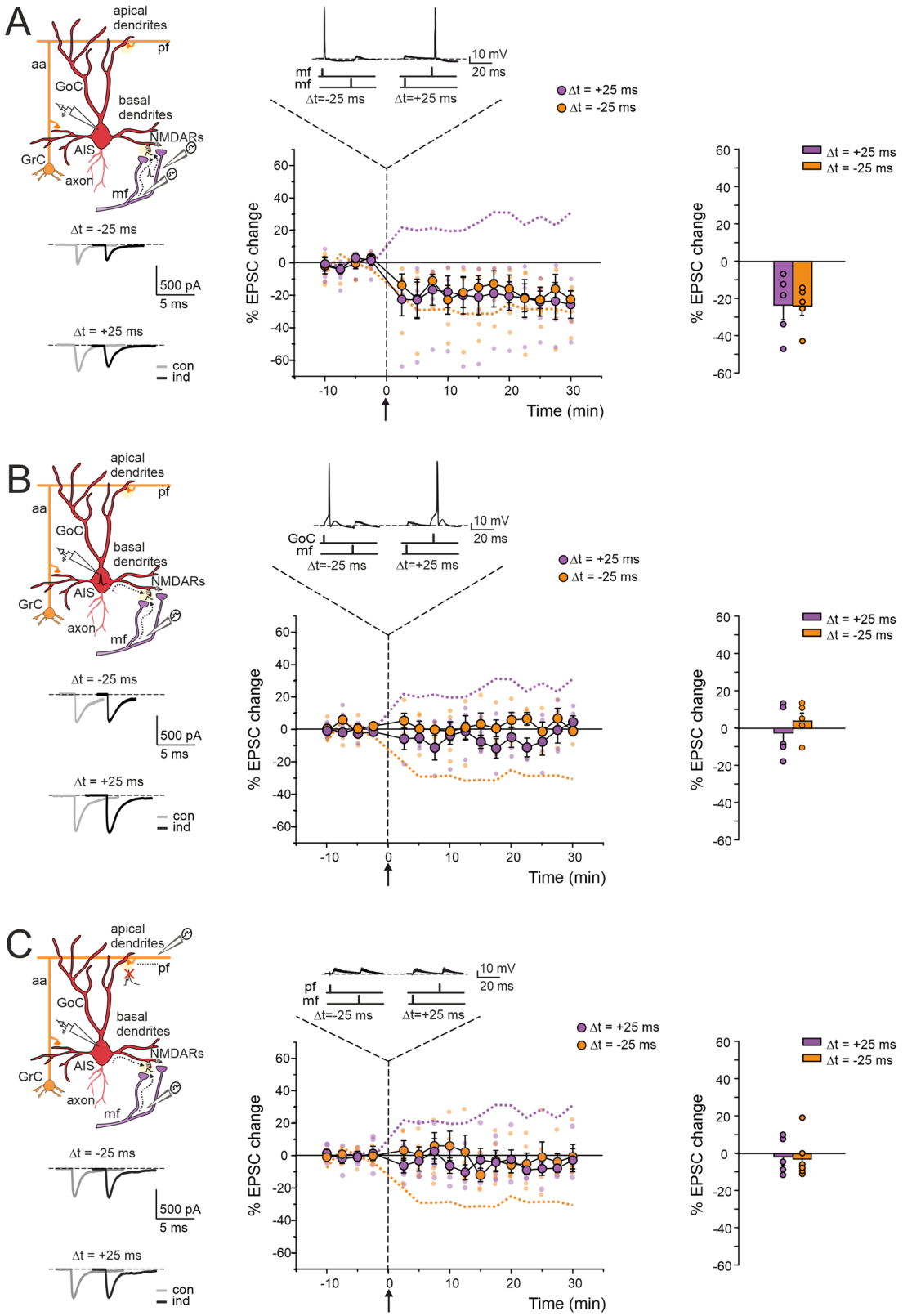


**Fig. 3 | STDP depends on APs elicited by pf stimulation.** Top left, schematic representations show the three different experimental conditions used to evaluate the role pf AP in STDP induction. Bottom left, EPSCs (average of 30 sweeps) evoked by mf stimulation are shown before (*con*-, gray traces) and 30 min after (*ind*-, black traces) STDP induction. The plots show the time course of average EPSC changes (large dots), with individual recordings overlaid (small dots). The arrows indicate the STDP induction time. Orange and purple dashed lines are replotted from Fig. 1B. Right, bar graphs show the average EPSC changes for Δt = −25 ms (orange) and Δt = +25 ms (purple). **A** STDP induction while activating only basal dendrites (mf-AP → mf-EPSP: $n = 5$, $N = 4$, $p = 0.03$; mf-EPSP → mf-AP: $n = 5$, $N = 5$, $p = 0.03$). **B** STDP induction with pf stimulation replaced by positive current injections into the soma (GoC-AP → mf-EPSP: $n = 5$, $N = 4$, $p = 0.29$; mf-EPSP → GoC-AP: $n = 5$, $N = 5$, $p = 0.69$). **C** STDP induction with a limited number of pf-elicited APs ( < 10 APs in 60 impulses; pf-EPSP → mf-EPSP: $n = 6$, $N = 5$, $p = 0.72$; mf-EPSP → pf-EPSP: $n = 5$, $N = 5$, $p = 0.54$). Mean ± SEM; Student's paired *t* test; some standard errors are small and fall inside the dots. All the illustrations have been created with CorelDRAW 2019.

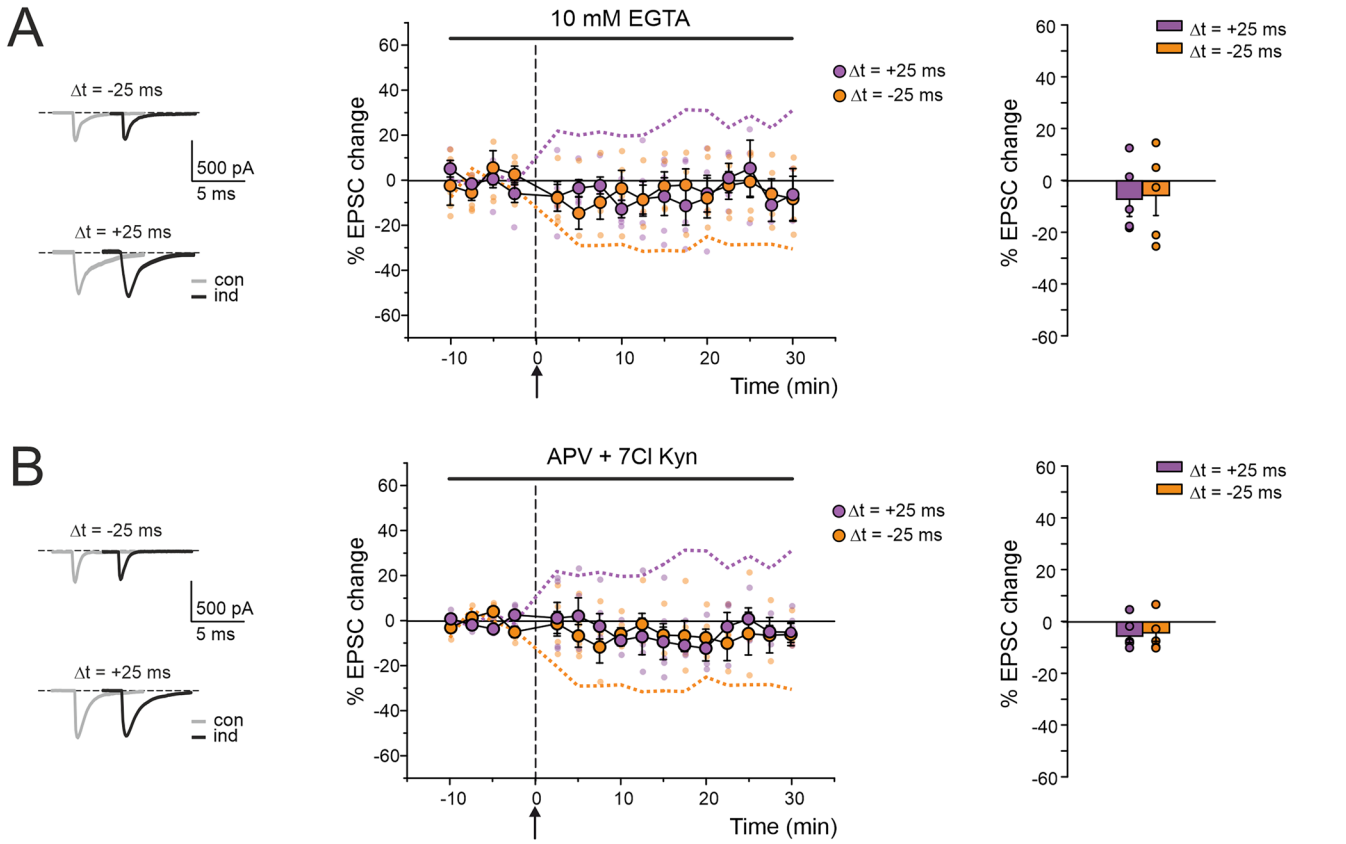


**Fig. 4 | STDP depends on postsynaptic $[Ca^{2+}]_i$ changes and NMDA receptor activation.** Left, EPSCs (average of 30 sweeps) evoked by mf stimulation are shown before (*con*-, gray traces) and 30 min after (*ind*-, black traces) STDP induction. The plots show the time course of average EPSC changes (large dots), with individual recordings overlaid (small dots). The arrows indicate the STDP induction time. Orange and purple dashed lines are replotted from Fig. 1B. Right, bar graphs show the average EPSC changes for Δt = −25 ms (orange) and Δt = +25 ms (purple). **A** STDP induction with 10 mM EGTA in the intracellular solution (black bar; pf-AP → mf-EPSP: $n = 5$, $N = 5$, $p = 0.44$; mf-EPSP → pf-AP: $n = 5$, $N = 4$, $p = 0.57$. **B** STDP induction during bath-application of NMDAR antagonists, APV and 7-Cl-Kyn (black bar; pf-AP → mf-EPSP: $n = 5$, $N = 4$, $p = 0.23$; mf-EPSP → pf-AP: $n = 5$, $N = 5$, $p = 0.24$). Mean ± SEM; Student's paired *t* test; some standard errors are small and fall inside the dots.

Finally, to demonstrate the requirements of pf-evoked APs in the STDP induction, we elicited only a limited number of pf-APs (<10 APs in 60 impulses) with pf-EPSP → mf-EPSP or mf-EPSP → pf-EPSP pairings (Fig. 3C). In this set of experiments, neither st-LTD (pf-EPSP → mf-EPSP: −2.7 ± 4.6%, $n = 6$, $N = 5$, Student's paired *t* test $p = 0.72$) nor st-LTP (mf-EPSP → pf-EPSP: −1.5 ± 4.4%, $n = 5$, $N = 5$, Student's paired *t* test $p = 0.54$) were induced. This indicates that APs are required and that presynaptic activation of basal dendrites via mf stimulation paired with subthreshold pf stimulation is insufficient to trigger STDP. Notably, the APs triggered by the EPSCs elicited by mf stimulation did not cause any differences in the magnitude of both st-LTP (0–10 mf APs: 11.1 ± 9.1%, $n = 7$, $N = 6$ vs. 11–60 mf APs: 19.4 ± 7.3%, $n = 4$; $N = 4$ Student's unpaired *t* test, $p = 0.55$) and st-LTD (0–10 mf APs: −22.4 ± 8.2%, $n = 6$, $N = 5$ vs. 11–60 mf APs: −15.1 ± 9.7%, $n = 5$; $N = 5$ Student's unpaired *t* test, $p = 0.58$; see also Supplementary Fig. 3).

In aggregate, these findings demonstrate that only APs elicited by pf stimulation serve as the necessary associative signals for the induction of STDP at active mf-GoC synapses.

### STDP requires postsynaptic calcium changes

To assess the STDP dependence on postsynaptic intracellular calcium ($[Ca^{2+}]_i$) changes, we increased the calcium buffering capacity of the intracellular solution (EGTA, 10 mM). Following the establishment of the whole-cell configuration, we allowed for a waiting period of approximately 15 min to ensure the effective perfusion of EGTA into the dendritic compartment before applying the STDP induction protocol. The presence of 10 mM EGTA in the pipette intracellular solution prevented both st-LTD (−6.1 ± 7.6%, $n = 5$, $N = 5$, Student's paired *t* test, $p = 0.44$) and st-LTP (−6.9 ± 5.9%, $n = 5$, $N = 4$, Student's paired *t* test, $p = 0.57$; Fig. 4A). These results indicate that mf-GoC STDP requires a postsynaptic calcium change for its induction, like other types of LTD and LTP observed at synapses in the central nervous system[18,21–23,67,68].

### STDP requires NMDA receptor activation

The NMDA receptor is a molecular coincidence detector of pre- and postsynaptic activity that requires two simultaneous conditions for its activation: glutamate binding and membrane depolarization. NMDA receptors are critical for the induction of long-term synaptic plasticity at several central synapses[52,58,61,63,69–71]. In cerebellar GoC, NMDA receptors are selectively located at mf-GoC postsynaptic sites[35], making basal dendrites suitable for NMDA-driven synaptic plasticity[23,33]. To test whether NMDA receptor activation is required for mf-GoC STDP, NMDA receptor antagonists, D-APV (100 µM) and 7-Cl Kyn (50 µM), were added to the extracellular Krebs' solution (Fig. 4B). Bath application of these drugs prevented the induction of both st-LTD (−4.7 ± 3.1%, $n = 5$, $N = 4$, Student's paired *t* test, $p = 0.23$;) and st-LTP (−4.9 ± 2.7%, $n = 5$, $N = 5$, Student's paired *t* test, $p = 0.24$). These results demonstrate that mf-GoC STDP consists of NMDA receptor-dependent st-LTP and NMDA receptor-dependent st-LTD, as it occurs at other synapses[22,65,70,72–75].

### STDP is shaped by the degree of NMDA receptor-driven membrane depolarization

According to model predictions[33], when pf-AP precedes the mf-EPSP, the latter aligns with the afterhyperpolarization (AHP) phase of the

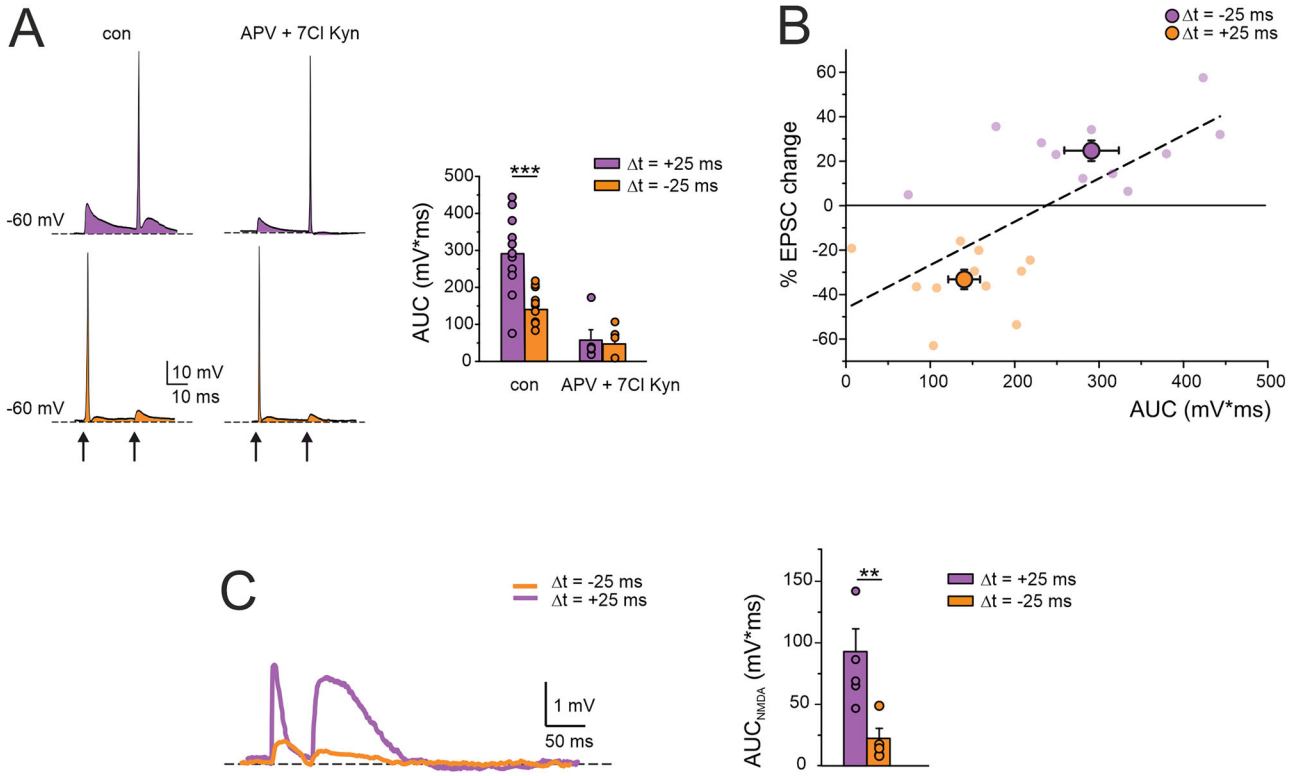


**Fig. 5 | STDP is determined by the degree of NMDA receptor-driven membrane depolarization. A** Sample traces (average of 60 sweeps) elicited during STDP induction showing AUC measured in response to mf-EPSP → pf-AP (purple) or pf-AP → mf-EPSP (orange) pairing. A similar experiment was repeated in the presence of NMDA receptor antagonists APV and 7-Cl-Kyn. The bar graphs show the average AUC value changes for Δt = −25 ms (orange) and Δt = +25 ms (purple) in control and with NMDA receptor antagonists (pf-AP → mf-EPSP: $n = 5$, $N = 5$, vs., $n = 11$, $N = 10$, $p = 0.013$; mf-EPSP → pf-AP: $n = 5$, $N = 4$, vs. $n = 11$, $N = 10$, $p = 0.0005$). **B** The plot shows the correlation between EPSC amplitude changes and the corresponding AUC value for each GoC recorded at Δt = −25 ms (large orange dots) and Δt = +25 ms (large purple dots), with individual recordings overlaid (small dots). Dotted line represents the linear fit to data points (Adj $R^2 = 0.44$, $n = 22$, $N = 20$, $p = 4.66*10^{-4}$). **C** Sample traces obtained as the difference between those measured in control condition and those obtained with NMDA receptor antagonists for Δt = −25 ms (orange) and Δt = +25 ms (purple). The bar graph shows a significantly smaller $AUC_{NMDA}$ at Δt = −25 ms (orange) than at Δt = +25 ms (purple; $n = 5$, $N = 5$, vs. $n = 5$, $N = 5$, $p = 0.008$). **, $p < 0.01$, ***, $p < 0.001$; Student's unpaired $t$ test.

backpropagating pf-AP, causing small membrane depolarization. In this scenario, NMDA channels unblock partially, resulting in limited $Ca^{2+}$ influx inducing st-LTD. Conversely, when pf-AP follows the mf-EPSP, the latter intercepts the backpropagating pf-AP causing high membrane depolarization, facilitating NMDA channel opening and causing a large $Ca^{2+}$ influx inducing st-LTP[33]. To investigate the STDP induction process, we measured the area under the curve (AUC, mV*ms) of traces recorded during the STDP induction (Fig. 5A). This analysis revealed significantly smaller AUCs when pairing pf-AP → mf-EPSP compared to those obtained when pairing mf-EPSP → pf-AP (153.4 ± 14.7 mV*ms, $n = 11$, $N = 10$, vs. 291.0 ± 32.5 mV*ms, $n = 11$, $N = 10$, Student's unpaired $t$ test, $p = 0.001$). Moreover, AUC values exhibited a positive linear correlation with changes in EPSC, specifically small AUC values corresponded to negative EPSC changes while high AUC values corresponded to positive EPSC changes ($R^2 = 0.44$, $n = 22$, $N = 20$, $p = 4.6*10^{-4}$; Fig. 5B). These findings imply that during pf-AP → mf-EPSP pairings a weaker membrane depolarization leads to st-LTD, while during mf-EPSP → pf-AP pairings a strong membrane depolarization leads to st-LTP[67,76,77].

Subsequently, we measured the AUC in those experiments where STDP stimulation protocol was delivered in the presence of NMDA receptor antagonists (Fig. 5A). When bath-applying NMDA receptor antagonists, a significant decrease in the AUC was observed for both pf-AP → mf-EPSP (51.5 ± 19.4 mV*ms, $n = 5$, $N = 5$, vs. 153.4 ± 14.7 mV*ms, $n = 11$, $N = 10$, Student's unpaired $t$ test, $p = 0.013$) and mf-EPSP → pf-AP pairings (58.5 ± 28.3 mV*ms, $n = 5$, $N = 4$, vs. 290.9 ± 32.5 mV*ms, $n = 11$, $N = 10$, Student's unpaired $t$ test, $p = 0.0005$). Notably, under NMDA receptor antagonists, these reduced membrane depolarizations were not associated with any plastic changes, reflecting the properties of NMDA receptors, which provide calcium to trigger both st-LTP and st-LTD.

The involvement of NMDA receptors during STDP induction was evaluated by delivering the stimulation protocol before and after applying NMDA receptor antagonists (D-APV, 100 μM, and 7-Cl Kyn, 50 μM) and then subtracting AUCs obtained in control condition from those obtained after the NMDA receptor blockade in order to isolate membrane potential changes solely attributable to NMDA receptor activation (Fig. 5C). We found a significantly smaller $AUC_{NMDA}$ for pf-AP → mf-EPSP than for mf-EPSP → pf-AP pairing (22.0 ± 8.6 mV*ms, $n = 5$, $N = 5$, vs 92.8 ± 18.5 mV*ms, $n = 5$, $N = 5$, Student's unpaired $t$ test, $p = 0.008$).

In summary, our findings indicate that mf-GoC plasticity depends on dynamic NMDA receptor unblocking during pairing, and the transition between st-LTD and st-LTP critically be contingent to the degree of membrane depolarization, which, in turn, is correlated with the extent of NMDA receptor activation.

### STDP is shaped by inhibition

Inhibitory signaling is known to constrain the time window within which synaptic inputs can summate and reach the AP threshold[78,79]. Since the induction of GoC st-LTD and st-LTP depends on the precise timing of pf-AP relative to mf-EPSP, inhibitory circuits may play a key role in affecting STDP. In a set of experiments, both $GABA_A$ and glycine receptor antagonists were omitted from the extracellular Krebs' solution (Fig. 6). Under these conditions, STDP was inverted, so that st-LTD occurred with mf-EPSP → pf-AP pairing (− 28.1 ± 2.8%, $n = 5$, $N = 5$, Student's paired $t$ test,

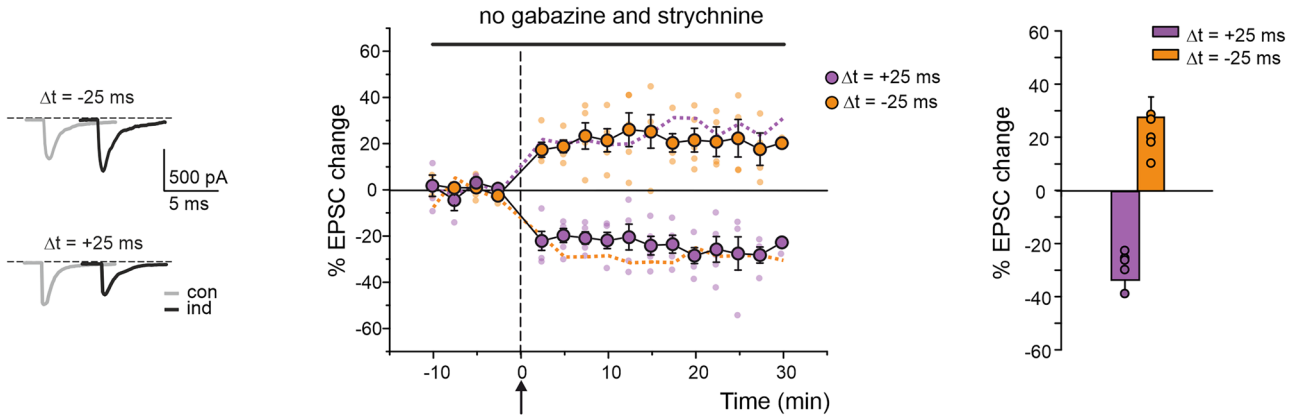


**Fig. 6 | The polarity of STDP is shaped by inhibition.** Left, EPSCs (average of 30 sweeps) evoked by mf stimulation are shown before (*con*-, gray traces) and 30 min after (*ind*-, black traces) STDP induction while omitting gabazine and strychnine from the extracellular solution. The plot shows the time course of average EPSC changes (large dots), with individual recordings overlaid (small dots; (mf-EPSP → pf-AP: $n = 5$, $N = 5$, $p = 0.006$; pf-AP → mf-EPSPP: $n = 5$, $N = 5$, $p = 0.002$; mean ± SEM; Student's paired $t$ test; some standard errors are small and fall inside the dots). The arrow indicates the STDP induction time. Orange and purple dashed lines are replotted from Fig. 1B. Right, bar graphs show the average EPSC changes for Δt = −25 ms (orange) and Δt = +25 ms (purple).

$p = 0.006$), whereas st-LTP occurred with pf-AP → mf-EPSP pairing (21.0 ± 3.3%, $n = 5$, $N = 5$, Student's paired $t$ test, $p = 0.002$).

These results indicate that inhibitory signals can exert a dramatic effect on mf-GoC STDP timing-rules, similar to what has been reported at cerebellar inputs[22] and neocortical synapses[80,81]. In the continuation of the work, only experiments in the presence of gabazine and strychnine have been performed.

### STDP is confined to the theta band

STDP critically depends on temporal relationships occurring within a specific range of spiking frequencies[58,82]. To better characterize this phenomenon, it is essential to explore the optimal input frequency range that facilitates its induction. We therefore applied pf-AP → mf-EPSP or mf-EPSP → pf-AP pairings repeated at 1, 6, and 10 Hz. It is worth noting that, assessing STDP at 20 Hz, would cause aliasing (i.e., the "aliasing" frequency at which the positive and negative phase coincide). As previously described, STDP was induced at a pairing frequency of 4 Hz (pf-AP → mf-EPSP: −33.6 ± 4.7%, $n = 6$, $N = 6$, Student's paired $t$ test, $p = 0.006$; mf-EPSP → pf-AP: 27.1 ± 7.4%, $n = 6$, $N = 5$, Student's paired $t$ test, $p = 0.01$). To investigate whether STDP is specifically tuned on the theta-band, we repeated the induction protocol at 6 Hz (Fig. 7A). Consistent with findings at mf-granule cell synapses[22] (see also Supplementary Fig. 4), pf-AP → mf-EPSP pairings at 6 Hz induced st-LTD (–27.5 ± 3.0%, $n = 5$, $N = 5$, Student's paired $t$ test, $p = 0.006$), whereas mf-EPSP → pf-AP pairings at 6 Hz induced st-LTP (19.3 ± 4.0%, $n = 5$, $N = 4$, Student's paired $t$ test, $p = 0.02$). The magnitude of these effects was comparable to those observed at 4 Hz (st-LTD: 4 Hz vs. 6 Hz, Student's unpaired $t$ test, $p = 0.33$; st-LTP: 4 Hz vs. 6 Hz, Student's unpaired $t$ test, $p = 0.40$).

Remarkably, at either 1 Hz (pf-AP → mf-EPSP: 2.3 ± 5.6%, $n = 5$, $N = 5$, Student's paired $t$ test, $p = 0.42$; mf-EPSP → pf-AP: −3.2 ± 5.4%, $n = 5$, $N = 5$, Student's paired $t$ test, $p = 0.63$) or 10 Hz (pf-AP → mf-EPSP: −5.6 ± 3.0%, $n = 5$, $N = 5$, Student's paired $t$ test, $p = 0.16$; mf-EPSP → pf-AP: 0.5 ± 5.8%, $n = 5$, $N = 5$, Student's paired $t$ test, $p = 0.97$) STDP disappeared (Fig. 7B, C).

These findings indicate that mf-GoC STDP occurs within a specific and restricted frequency range, supporting its role in confining synaptic modifications to the theta-band (4–8 Hz; Fig. 7D).

### STDP expression is postsynaptic

To investigate the locus of STDP expression, EPSCs were evoked using paired pulse (PP) stimulation (interstimulus interval of 20 ms) of the mf bundle at 0.2 Hz for 10 min in control and 30 min after STDP induction (Fig. 8A). In these experiments, the magnitude of both st-LTD and st-LTP was consistent with our previous results using single-pulse (SP) stimulation (SP, st-LTD: −33.6 ± 4.7%, $n = 6$, $N = 6$, vs. PP, st-LTD: −34.5 ± 7.6%, $n = 5$, $N = 5$, Student's unpaired $t$ test, $p = 0.91$; SP, st-LTP: 27.1 ± 7.4%, $n = 6$, $N = 5$, vs. PP, st-LTP: 21.7 ± 5.5%, $n = 5$, $N = 4$, Student's unpaired $t$ test, $p = 0.58$). The PPR and the CV of EPSCs were analyzed (see Methods for details). PPR is considered to reflect changes in the probability of transmitter release in response to a couple of stimuli[83], while CV provides information about the probability of quantal transmitter release upon repeated stimulation[84,85]. However, it is important to note that CV analysis relies on several underlying assumptions, including binomial vesicle release and a purely monosynaptic connection[86,87]. In our experimental configuration, some of these assumptions—particularly the variability in the number of mfs recruited by the stimulating electrode—may be partially violated. Therefore, the interpretation of CV changes should be viewed as supportive but not definitive evidence regarding the locus of STDP expression.

After the induction of st-LTD and st-LTP, the PPR did not show significant changes (Fig. 8B; st-LTD: −3.8 ± 10.3%, $n = 5$, $N = 5$, Student's paired $t$ test, $p = 0.59$; st-LTP: −2.3 ± 8.1%, $n = 5$, $N = 4$ Student's paired $t$ test, $p = 0.52$). Then we examined changes in the CV of EPSCs following the STDP induction. No significant changes in CV were observed either in st-LTD or st-LTP (Fig. 8B; st-LTD: 2□1 ± 0.8%, $n = 5$, $N = 5$, Student's paired $t$ test, $p = 0.85$; st-LTP: −5.9 ± 7.8%, $n = 5$, $N = 4$, Student's paired $t$ test, $p = 0.55$). The absence of changes in CV and PPR after the induction of long-term synaptic plasticity suggests a change in quantum size[51,84,88] and thereby a postsynaptic expression mechanism for mf-GoC STDP.

## Discussion

In this work we report the first evidence for STDP at the cerebellar mf-GoC synapse, a form of plasticity that was recently predicted by computational modeling[33]. According to the Hebbian principle of coincidence detection between presynaptic and postsynaptic activity, mf-GoC STDP consisted anti-symmetric st-LTP and st-LTD that were induced by repeated mf-pf pairing within *a* ± 50 ms time window. The phase difference between mf-EPSPs and APs elicited by pf activity determined the direction and magnitude of mf-GoC STDP. The induction process required repeated stimulation cycles at 4 Hz along with NMDAR activation and cytoplasmic calcium concentration changes. Beside similarities with the general mechanisms observed at synapses of neocortex, hippocampus, striatum, and cerebellum[22,59,61,89–99], mf-GoC STDP shows peculiarities related to the specific cellular and circuit organization and function.

GoCs have a distinct dendritic architecture, with basal dendrites confined into the granular layer receiving excitatory input from mfs and

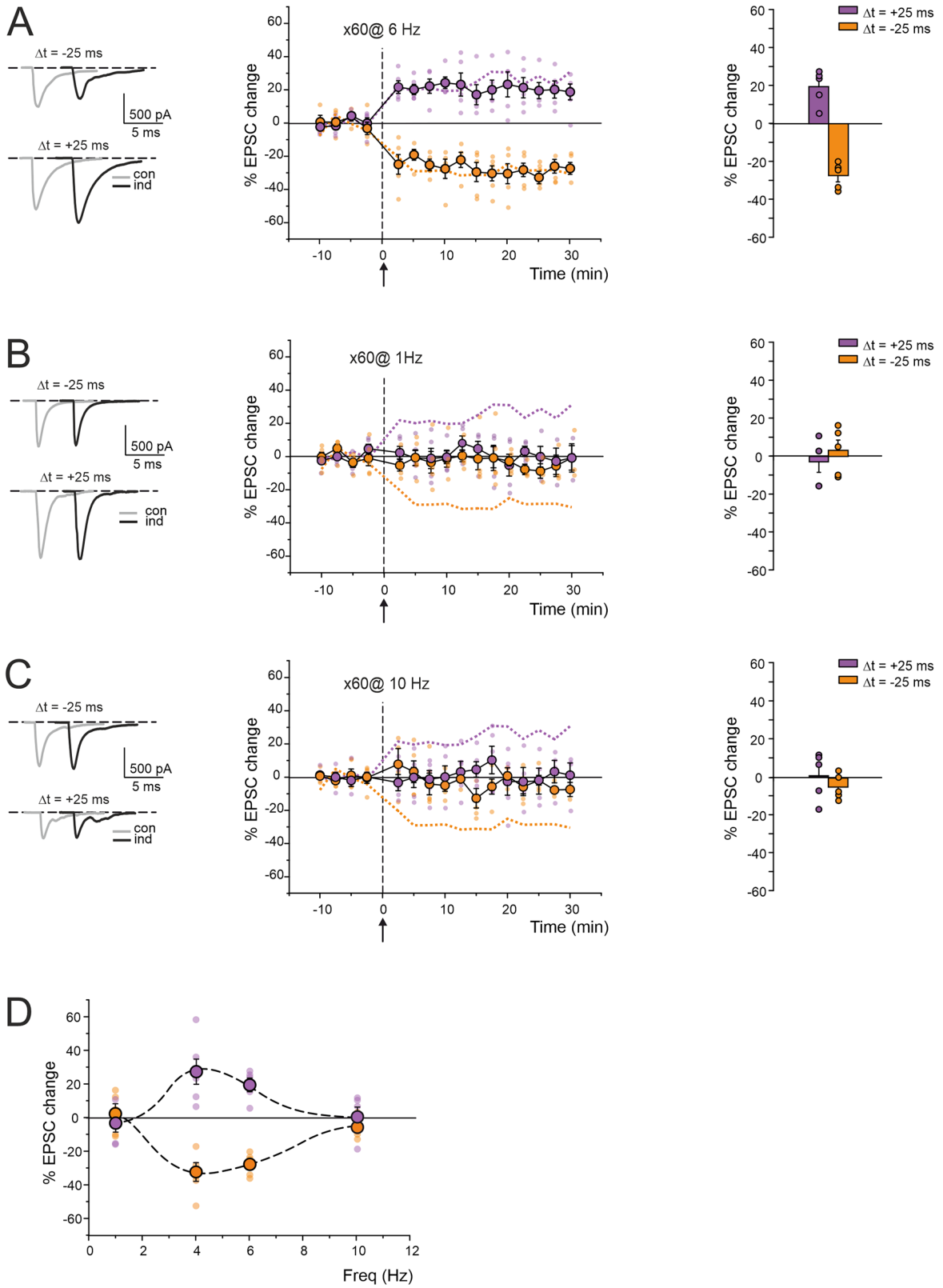


**Fig. 7 | STDP depends on the pairing frequency.** Left, EPSCs (average of 30 sweeps) evoked by mf stimulation are shown before (*con*-, gray traces) and 30 min after (*ind*-, black traces) STDP induction at 6, 1 or 10 Hz. The plots show the time course of average EPSC changes (large dots), with individual recordings overlaid (small dots). The arrows indicate the STDP induction time. Orange and purple dashed lines are replotted from Fig. 1B. Right, bar graphs show the average EPSC changes for Δt = −25 ms (orange) and Δt = +25 ms (purple). **A** STDP induction at 6 Hz (pf-AP → mf-EPSP: $n = 5$, $N = 5$, $p = 0.006$; mf-EPSP → pf-AP: $n = 5$, $N = 4$, $p = 0.02$). **B** STDP induction at 1 Hz (pf-AP → mf-EPSP: $n = 5$, $N = 5$, $p = 0.42$; mf-EPSP → pf-AP: $n = 5$, $N = 5$, $p = 0.63$). **C** STDP induction at 10 Hz (pf-AP → mf-EPSP: $n = 5$, $N = 5$, $p = 0.16$; mf-EPSP → pf-AP: $n = 5$, $N = 5$, $p = 0.97$). **D** STDP frequency curve shows EPSC amplitude changes in individual recordings 30 min after induction (small dots), and average EPSC changes (large dots). Mean ± SEM; Student's paired *t* test; some standard errors are small and fall inside the dots.

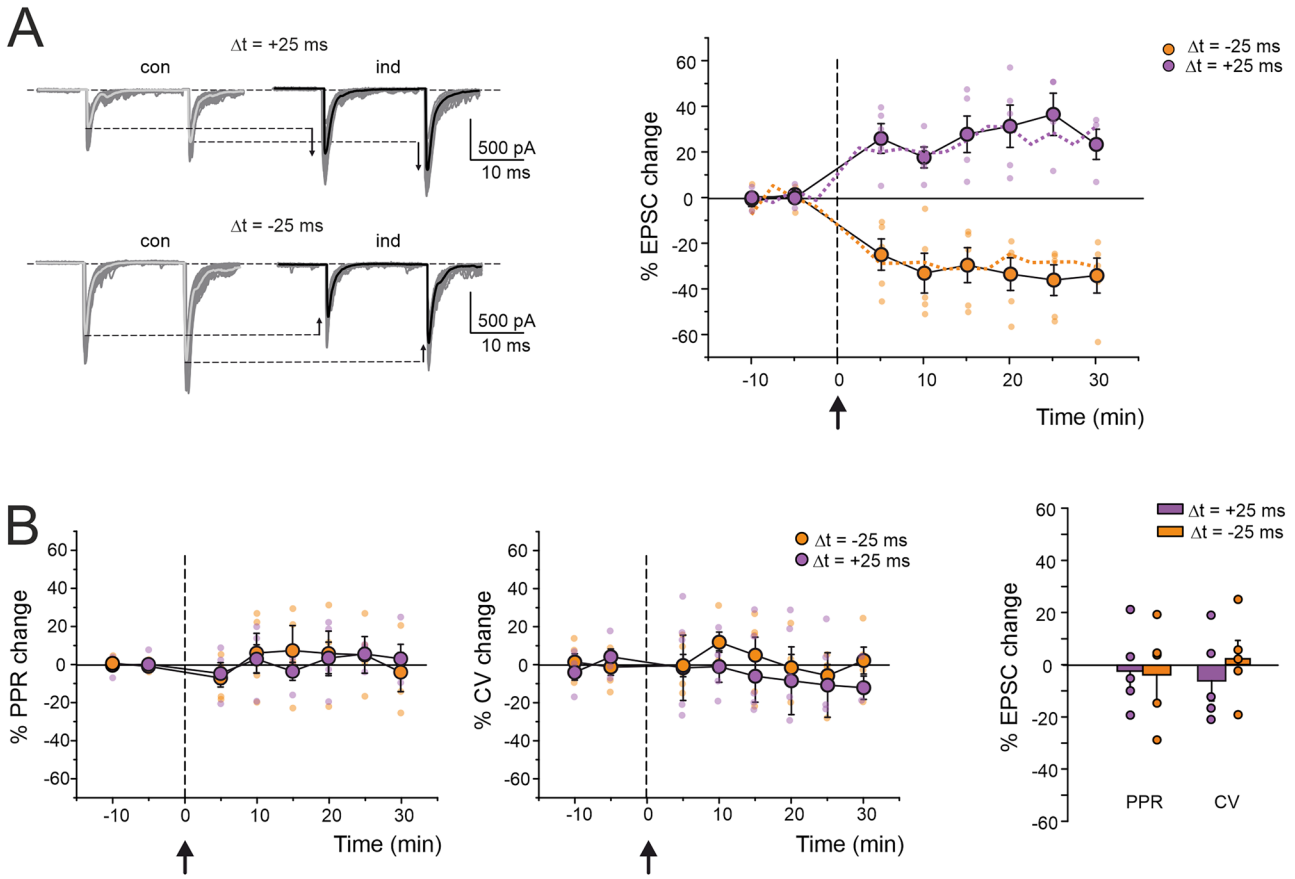


**Fig. 8 | CV and PPR analysis during STDP expression. A** Individual EPSCs (60 sweeps) evoked by PP stimulation of mf before (*con*) and 30 min after (*ind*) STDP induction are shown superimposed (thin traces) along with their respective averages (thick traces). The plots show the time course of average EPSC changes (large dots), with individual recordings overlaid (small dots). The arrows indicate the STDP induction time. Note that the magnitude of both st-LTD (orange dots) and st-LTP (purple dots) was similar to that obtained with SP stimulation (orange and purple dashed lines, replotted from Fig. 1B; SP, st-LTD: $n = 6$, $N = 6$, vs. PP, st-LTD: $n = 5$, $N = 5$, $p = 0.91$; SP, st-LTP: $n = 6$, $N = 5$, vs. PP, st-LTP: $n = 5$, $N = 4$, $p = 0.58$; mean ± SEM; Student's unpaired *t*-test; some standard errors are small and fall inside the dots). **B** Time course of PPR and CV changes after STDP induction (large dots), with individual recordings overlaid (small dots; PPR, st-LTD: $n = 5$, $N = 5$, $p = 0.59$; PPR st-LTP: $n = 5$, $N = 4$, $p = 0.52$; CV, st-LTD: $n = 5$, $N = 5$, $p = 0.85$; CV, st-LTP: $n = 5$, $N = 4$, $p = 0.55$; mean ± SEM; Student's paired *t* test; some standard errors are small and fall inside the dots). The arrows indicate the STDP induction time. Right, bar graphs show the average PPR and CV changes for Δt = −25 ms (orange) and Δt = +25 ms (purple).

ascending granule cell axons, and apical dendrites extending into the molecular layer, where they are excited by pfs[35]. This organization suggests that synapses onto different dendritic regions convey distinct types of information, which might be integrated in different ways. Consistent with this idea basal synapses could operate by direct depolarization of the somatic compartment, while integration of apical synaptic inputs is thought to occur through generation of dendritic spikes. Several studies have emphasized the importance of dendritic synapse location for STDP induction in cortical pyramidal cells[66,70,100,101]. Remarkably, this work is the first to demonstrate this principle in cerebellar neurons. We found that pairings of EPSPs and APs evoked by stimulating mfs did not yield anti-symmetric Hebbian STDP, leading to LTD instead as the sole expression of plasticity. Similarly, when APs were directly generated at the soma by injecting a positive current, plasticity did not occur. Thus, the emerging picture is that synaptic location has a profound impact on learning rules during mf-Goc STDP. These findings parallel the distinct roles that basal and apical inputs are believed to play in synaptic integration. In addition to that, we provide direct evidence showing that APs elicited by pf stimulation serve as the required associative signals for the induction of STDP at mf-GoC synapses. In fact, basal dendrite activation via mf stimulation paired with subthreshold pf stimulation (only EPSP) is not sufficient to trigger neither st-LTP or st-LTD.

This implies that local depolarization at the mf-GoC synapses during pairing, which is essential for NMDA receptor activation and subsequent STDP induction, is influenced not only by the temporal order of mf-evoked EPSPs and pf-driven APs but also by the specific compartment where APs are initiated. Therefore, biophysical properties of dendrites, that spatially regulate AP, concur to establish the STDP learning rules. GoCs contain a rich assortment of voltage-gated ion channels that promote and regulate AP backpropagation. In particular, the apical and basal dendrites show a diverse array of $Ca^{2+}$ channels (R-, N-, and T-type) and calcium-dependent potassium channels (BK- and SK-type)[30,33,38]. Notably, simulations mimicking experiments on the pharmacological blockade of $Ca^{2+}$ channels show that inhibiting apical dendritic APs can prevent mf-GoC STDP[33,66] (see also Supplementary Fig. 2).

In summary, apical dendritic properties exert powerful control over the modulation of mf inputs during GoC STDP induction. This form of STDP might, therefore, be better defined as dendritic-spike-dependent plasticity, as it depends more on the timing of mf input relative to apical dendritic AP than on the timing of somatic or basal dendritic APs. Thus, the extent and duration of depolarization associated with dendritic APs could differ among dendritic compartments, adding a new level of complexity in which the STDP induction (or eventually the sign and magnitude of plasticity) will depend on dendritic AP generation. Finally, as dendritic APs can be controlled locally via synaptic inhibition, the activity state of surrounding excitatory and inhibitory networks will play a crucial role in STDP induction.

NMDA receptors were functionally identified at the mf-GoC synapse[35] making basal dendrites suitable for NMDA receptor-driven synaptic plasticity[33]. We found that STDP depends on NMDA receptor activation since it was prevented by application of selective NMDA receptor antagonists. Moreover, as in classical NMDA receptor-dependent forms of STDP, mf-GoC STDP was blocked by increasing the cytoplasmic buffering capacity[20–23,61,68,77]. Additionally, slow NMDA channel kinetics[18,102,103] can explain the STDP time window. When a pf input follows a mf input, this latter intercepts the upstroke of backpropagating AP, causing high membrane depolarization. This, in turn, facilitates NMDA channel opening, leading to a significant increase in associated $Ca^{2+}$ influx in basal dendrites, thus inducing st-LTP[22,33,69]. When a pf input precedes a mf input, this latter falls in the AHP region of the backpropagating AP. NMDA channels fail to properly unblock, resulting in minimal receptor activation and limited calcium influx, leading to st-LTD[22,33,52,104]. Indeed, these mechanisms, when introduced in the GoC computational model of[33] and coupled with the Shouval-Bear equations[52], allowed us to simulate mf-GoC STDP.

GoCs receive GABAergic synaptic inhibition exclusively onto basal dendrites from other GoCs[31–33]. This reciprocal inhibition is believed to drive synchronous oscillations in the GoC network[105–108], and promote the acquisition of mf engrams[109]. Intriguingly, we found that it can also invert the polarity of mf-GoC STDP. In detail, when a pf input follows a mf input, the latter intercepts the upstroke of the backpropagating AP, causing strong membrane depolarization. This, in turn, triggers an inward hyperpolarizing chloride current, which reduces NMDA receptor activation and the associated calcium influx, leading to st-LTD. When a pf input precedes a mf input, the latter occurs within the AHP region of the backpropagating AP, failing to properly sustain membrane depolarization. In this scenario, chloride acts as a depolarizing current because the GoC membrane potential is more hyperpolarized than the chloride reversal potential. This, in turn, facilitates NMDA receptor channel opening, leading to a significant increase in calcium influx, thus inducing st-LTP.

Inhibitory neurons are well known for regulating spike timing across various brain circuits[22,78,79,81,110,111]. However, their role in controlling STDP has remained unclear. Here, we report that unblocked synaptic inhibition exerts powerful control over STDP timing rules at mf-GoC synapses. Our results reconcile the different reported polarity of the STDP, which depends on the use of inhibitory antagonists or not[22,80,81,93,112,113]. Therefore, inhibitory circuits appear to act as a Hebbian/anti-Hebbian switch.

At the cerebellar input stage, in addition to classical LTP and LTD, which depend on tetanization frequency—LTD being evoked at low frequencies (1 Hz) and LTP at high frequencies (100 Hz)[21]—it is also possible to robustly induce both LTP and LTD within the theta-band frequency range (6 Hz; Sgritta et al., 2017; see also Supplementary Fig. 4). At the same time, mf- GoC STDP operates primarily in a restricted firing frequency (4-6 Hz). Indeed, neither st-LTP nor st-LTD was induced at a frequency of 1 or 10 Hz. This result confirms that the relative timing of EPSPs and backpropagating AP is only one of several factors within a multifactor plasticity rule[89,92]. Low-frequency oscillations seem predominant in the cerebellar networks and neurons in the granular layer such as GoCs may operate in the theta-band frequency[28,114,115]. Thus, in the granular layer, STDP at mf-GoC synapse could provide a way to coordinate learning and memory during specific functional states, such as voluntary movement, resting attentiveness and sleep[116,117], with the activity generated in extracerebellar structures, like neocortex and striatum, which show coherent oscillations with the cerebellum[28,118–120]. Specific experiments could now be designed to investigate the implications of mossy fiber- Golgi cell STDP for cerebellar learning[121].

Evidence at different brain synapses reports that both pre- and postsynaptic changes can occur during STDP[17,60,71,122–126]. At the mf-GoC synapse, PPR and CV remained unchanged after induction[21,22,51,127–130], suggesting a postsynaptic mechanism. Interestingly, at the neighboring mf-GoC synapses that share the same mf terminals, STDP has a mixed presynaptic and postsynaptic expression[22]. Therefore, the STDP at the two synapses have at least in part different expression mechanisms, a fact that could have computational implications that remains to investigated[131–134].

This form of anti-symmetric Hebbian STDP, driven by apical-to-basal dendritic communication under NMDA receptor control and regulated by the local inhibitory circuit, places GoCs in a pivotal position to regulate information flow through the granular layer. Mossy fiber bursts of varying duration and frequency can induce long-term synaptic plasticity at mf-GrC synapses[20,21], at mf-GoC synapses[23], and at GoC-GrC synapses[135], eventually fine-tuning granule cell excitation. Beyond burst-induced plasticity, mf-GoC STDP emerges as a crucial mechanism for reorganizing granular layer neurotransmission depending on phase differences with the other major cerebellar fiber system, the pfs. By modifying synaptic inhibition of granule cells, it can dynamically regulate spike-timing at the cerebellar input stage. Furthermore, since pfs integrate signals from distant cerebellar regions, mf-GoC STDP may coordinate cerebellar processing across multiple modules. Specifically, if activity in a parallel fiber module systematically precedes that of a mossy fiber module, GoC inhibition in the latter is reduced by st-LTD, and vice versa. This suggests that associative interactions between cerebellar modules can influence local processing through mf-GoC STDP.

Both mf-GoC STDP and mf-granule cell STDP operate within the theta-frequency range, suggesting a strong modulation by slow brain rhythms and resonance phenomena in the granular layer. Theta-band oscillations have been observed in GoCs and granule cells[28,114,115], and mf-GoC STDP could therefore contribute to aligning cerebellar function with global network states, including voluntary movement, attentiveness, and sleep.

In conclusion, long-term synaptic changes in GoCs, shaped by temporally correlated mossy fiber and parallel fiber inputs, could have profound implications for granular layer processing. By orchestrating spatio-temporal reconfiguration of inhibition, mf-GoC STDP may contribute to cerebellar adaptive filtering and memory formation, as postulated by theoretical models[136] and increasingly supported by experimental and computational studies[121]. Further research, including large-scale network simulations, will be crucial to fully elucidate the role of mf-GoC STDP in cerebellar learning.

## Data availability

All source data used for graphs can be found in Supplementary Data 1.

## Code availability

The model is available on ModelDB (https://modeldb.science/2017007 (password: 215644)) and on the EBRAINS knowledge Graph.

Requests for materials should be addressed to F.P.

Received: 24 June 2024; Accepted: 1 May 2025;
Published online: 12 May 2025

## References

1. Bliss, T. V. P., Collingridge, G. L. & Morris, R. G. M. Synaptic plasticity in health and disease: Introduction and overview. *Philos. Trans. R. Soc. B Biol. Sci.* **369**, 0129 (2014).
2. Volianskis, A. et al. Long-term potentiation and the role of N-methyl-D-aspartate receptors. *Brain Res* **1621**, 5–16 (2015).
3. Magee, J. C. & Grienberger, C. Synaptic Plasticity Forms and Functions. *Ann. Rev. Neurosci.* **43**, 95–117 (2020).
4. Marr, D. A theory of cerebellar cortex. *J. Physiol.* **202**, 437–470 (1969).
5. Albus, J. S. A theory of cerebellar function. *Math. Biosci.* **10**, 25–61 (1971).
6. Ito, M. Control of mental activities by internal models in the cerebellum. *Nat. Rev. Neurosci.* **9**, 304–313 (2008).
7. Stoodley, C. J. & Schmahmann, J. D. Functional topography in the human cerebellum: A meta-analysis of neuroimaging studies. *Neuroimage* **44**, 489–501 (2009).
8. Bellebaum, C., Daum, I. & Suchan, B. Mechanisms of cerebellar contributions to cognition in humans. *Wiley Interdiscip. Rev. Cogn. Sci.* **3**, 171–184 (2012).

9. Sokolov, A. A., Miall, R. C. & Ivry, R. B. The Cerebellum: Adaptive Prediction for Movement and Cognition. *Trends Cogn. Sci.* **21**, 313–332 (2017).
10. D'Angelo, E. The cerebellum gets social. *Science* **363**, 229 (2019).
11. Ciapponi, C. et al. Variations on the theme: focus on cerebellum and emotional processing. *Front. Syst. Neurosci.* **17**, 1185752 (2023).
12. Zhang, W. & Linden, D. J. Long-term depression at the mossy fiber-deep cerebellar nucleus synapse. *J. Neurosci.* **26**, 6935–6944 (2006).
13. Pugh, J. R. & Raman, I. M. Nothing can be coincidence: synaptic inhibition and plasticity in the cerebellar nuclei. *Trends Neurosci* **32**, 170–177 (2009).
14. Gao, Z., Van Beugen, B. J. & De Zeeuw, C. I. Distributed synergistic plasticity and cerebellar learning. *Nat. Rev. Neurosci.* **13**, 619–635 (2012).
15. D'Angelo, E. The organization of plasticity in the cerebellar cortex: from synapses to control. *Prog. Brain Res.* **210**, 31–58 (2014).
16. Hansel, C., Linden, D. J. & D'Angelo, E. Beyond parallel fiber LTD: The diversity of synaptic and non-synaptic plasticity in the cerebellum. *Nat. Neurosci.* **4**, 467–475 (2001).
17. Linden, D. J. The expression of cerebellar LTD in culture is not associated with changes in AMPA-receptor kinetics, agonist affinity, or unitary conductance. *Proc. Natl. Acad. Sci.* **98**, 14066–14071 (2001).
18. D'Angelo, E., Rossi, P., Armano, S. & Taglietti, V. Evidence for NMDA and mGLU receptor-dependent long-term potentiation of mossy fiber-granule cell transmission in rat cerebellum. *J. Neurophysiol.* **81**, 277–287 (1999).
19. Armano, S., Rossi, P., Taglietti, V. & D'angelo, E. Long-term potentiation of intrinsic excitability at the mossy fiber-granule cell synapse of rat cerebellum. *J. Neurosci.* **20**, 5208–5216 (2000).
20. Gall, D. et al. Intracellular calcium regulation by burst discharge determines bidirectional long-term synaptic plasticity at the cerebellum input stage. *J. Neurosci.* **25**, 4813–4822 (2005).
21. D'Errico, A., Prestori, F. & D'Angelo, E. Differential induction of bidirectional long-term changes in neurotransmitter release by frequency-coded patterns at the cerebellar input. *J. Physiol.* **587**, 5843–5857 (2009).
22. Sgritta, M., Locatelli, F., Soda, T., Prestori, F. & D'Angelo, E. U. Hebbian spike-timing dependent plasticity at the cerebellar input stage. *J. Neurosci.* **37**, 2809–2823 (2017).
23. Locatelli, F. et al. Calcium channel-dependent induction of long-term synaptic plasticity at excitatory golgi cell synapses of cerebellum. *J. Neurosci.* **41**, 3307–3319 (2021).
24. Golgi, C. The neuron doctrine-theory and facts. *Nobel Lectures, Physiology or Medicine, 1901–1921* 189–217 (Elsevier, New York, 1967).
25. Galliano, E., Mazzarello, P. & D'Angelo, E. Discovery and rediscoveries of Golgi cells. *J. Physiol.* **588**, 3639–3655 (2010).
26. Bentivoglio, M. et al. The original histological slides of camillo Golgi and his discoveries on neuronal structure. *Front. Neuroanat.* **13**, 3 (2019).
27. D'Angelo, E. & De Zeeuw, C. I. Timing and plasticity in the cerebellum: focus on the granular layer. *Trends Neurosci*. **32**, 30–40 (2009).
28. D'Angelo, E. The critical role of Golgi cells in regulating spatio-temporal integration and plasticity at the cerebellum input stage. *Front. Neurosci.* **2**, 35–46 (2009).
29. Sudhakar, S. K. et al. Spatiotemporal network coding of physiological mossy fiber inputs by the cerebellar granular layer. *PLoS Comput. Biol.* **13**, e1005754 (2017).
30. Vervaeke, K., Lorincz, A., Nusser, Z. & Silver, R. A. Gap junctions compensate for sublinear dendritic integration in an inhibitory network. *Science* **335**, 1624–1628 (2012).
31. Hull, C. & Regehr, W. G. Identification of an inhibitory circuit that regulates cerebellar golgi cell activity. *Neuron* **73**, 149–158 (2012).
32. Eyre, M. D. & Nusser, Z. Only a minority of the inhibitory inputs to cerebellar Golgi cells originates from local GABAergic cells. *eNeuro* **3**, ENEURO.0055-16 (2016).
33. Masoli, S., Ottaviani, A., Casali, S. & D'Angelo, E. Cerebellar Golgi cell models predict dendritic processing and mechanisms of synaptic plasticity. *PLoS Comput. Biol.* **16**, e1007937 (2020).
34. Prestori, F., Mapelli, L. & D'Angelo, E. Diverse Neuron Properties and Complex Network Dynamics in the Cerebellar Cortical Inhibitory Circuit. *Front. Mol. Neurosci.* **12**, 492015 (2019).
35. Cesana, E. et al. Granule cell ascending axon excitatory synapses onto golgi cells implement a potent feedback circuit in the cerebellar granular layer. *J. Neurosci.* **33**, 12430–12446 (2013).
36. Apps, R. & Hawkes, R. Cerebellar cortical organization: a one-map hypothesis. *Nat. Rev. Neurosci.* **10**, 670–681 (2009).
37. Apps, R. et al. Cerebellar modules and their role as operational cerebellar processing units. *Cerebellum* **17**, 654–682 (2018).
38. Rudolph, S., Hull, C. & Regehr, W. G. Active dendrites and differential distribution of calcium channels enable functional compartmentalization of golgi cells. *J. Neurosci.* **35**, 15492–15504 (2015).
39. Zeilhofer, H. U. et al. Glycinergic neurons expressing enhanced green fluorescent protein in bacterial artificial chromosome transgenic mice. *J. Comp. Neurol.* **482**, 123–141 (2005).
40. Forti, L., Cesana, E., Mapelli, J. & D'Angelo, E. Ionic mechanisms of autorhythmic firing in rat cerebellar Golgi cells. *J. Physiol.* **574**, 711–729 (2006).
41. Dugué, G. P., Dumoulin, A., Triller, A. & Dieudonné, S. Target-dependent use of coreleased inhibitory transmitters at central synapses. *J. Neurosci.* **25**, 6490–6498 (2005).
42. Neher, E. Correction for liquid junction potentials in patch clamp experiments. *Methods Enzymol* **207**, 123–131 (1992).
43. Simat, M., Parpan, F. & Fritsch, J. M. Heterogeneity of glycinergic and gabaergic interneurons in the granule cell layer of mouse cerebellum. *J. Comp. Neurol.* **500**, 71–83 (2007).
44. Dumontier, D., Mailhes-Hamon, C., Supplisson, S. & Dieudonné, S. Neurotransmitter content heterogeneity within an interneuron class shapes inhibitory transmission at a central synapse. *Front. Cell Neurosci.* **16**, 1060189 (2023).
45. Dieudonné, S. & Dumoulin, A. Serotonin-driven long-range inhibitory connections in the cerebellar cortex. *J. Neurosci.* **20**, 1837–1848 (2000).
46. Hirono, M., Nagao, S., Yanagawa, Y. & Konishi, S. Monoaminergic modulation of GABAergic transmission onto cerebellar globular cells. *Neuropharmacology* **118**, 79–89 (2017).
47. Miyazaki, T., Yamasaki, M., Tanaka, K. F. & Watanabe, M. Compartmentalized input–output organization of lugaro cells in the cerebellar cortex. *Neuroscience* **462**, 89–105 (2021).
48. Kanichay, R. T. & Silver, R. A. Synaptic and cellular properties of the feedforward inhibitory circuit within the input layer of the cerebellar cortex. *J. Neurosci.* **28**, 8955–8967 (2008).
49. Tabuchi, S., Gilmer, J. I., Purba, K. & Person, A. L. Pathway-specific drive of cerebellar golgi cells reveals integrative rules of cortical inhibition. *J. Neurosci.* **39**, 1169–1181 (2019).
50. Sillitoe, R. V., Chung, S. H., Fritschy, J. M., Hoy, M. & Hawkes, R. Golgi cell dendrites are restricted by purkinje cell stripe boundaries in the adult mouse cerebellar cortex. *J. Neurosci.* **28**, 2820–2826 (2008).
51. Sola, E., Prestori, F., Rossi, P., Taglietti, V. & D'Angelo, E. Increased neurotransmitter release during long-term potentiation at mossy fibre-granule cell synapses in rat cerebellum. *J. Physiol.* **557**, 843–861 (2004).
52. Shouval, H. Z., Bear, M. F. & Cooper, L. N. A unified model of NMDA receptor-dependent bidirectional synaptic plasticity. *Proc. Natl. Acad. Sci.* **99**, 10831–10836 (2002).

53. Casali, S., Tognolina, M., Gandolfi, D., Mapelli, J. & D'Angelo, E. Cellular-resolution mapping uncovers spatial adaptive filtering at the rat cerebellum input stage. *Commun. Biol.* **3**, 635 (2020).
54. Hines, M. L., Davison, A. P. & Muller, E. NEURON and Python. *Front. Neuroinform.* **3**, 3389 (2009).
55. Dan, Y. & Poo, M.-M. Review spike timing-dependent plasticity of neural circuits (Fig. 1), which are on the order of tens of milliseconds. *Neuron* **44**, 23–30 (2004).
56. Caporale, N. & Dan, Y. Spike timing–dependent plasticity: a hebbian learning rule. *Annu. Rev. Neurosci.* **31**, 25–46 (2008).
57. Markram, H., Gerstner, W. & Sjöström, P. J. Spike-timing-dependent plasticity: A comprehensive overview. *Front. Syn. Neurosci.* **4**, 2 (2012).
58. Markram, H., Gerstner, W. & Sjöström, P. J. A history of spike-timing-dependent plasticity. *Front. Syn. Neurosci.* **3**, 4 (2011).
59. Feldman, D. E. The spike-timing dependence of plasticity. *Neuron* **75**, 556–571 (2012).
60. Andrade-Talavera, Y., Fisahn, A. & Rodríguez-Moreno, A. Timing to be precise? An overview of spike timing-dependent plasticity, brain rhythmicity, and glial cells interplay within neuronal circuits. *Mol. Psychiatry* https://doi.org/10.1038/s41380-023-02027-w (2023).
61. Bi, G. Q. & Poo, M. M. Synaptic modifications in cultured hippocampal neurons: dependence on spike timing, synaptic strength, and postsynaptic cell type. *J. Neurosci.* **18**, 10464–10472 (1998).
62. Bi, G. Q. & Wang, H. X. Temporal asymmetry in spike timing-dependent synaptic plasticity. *Physiol. Behav.* **77**, 551–555 (2002).
63. Debanne, D. & Inglebert, Y. Spike timing-dependent plasticity and memory. *Curr. Opin. Neurobiol.* **80**, 102707 (2023).
64. Kepecs, A., Van Rossum, M. C. W., Song, S. & Tegner, J. Spike-timing-dependent plasticity: common themes and divergent vistas. *Biol. Cyber.* **87**, 446–458 (2002).
65. Sjöström, P. J. & Nelson, S. B. Spike timing, calcium signals and synaptic plasticity. *Curr. Opin. Neurobiol.* **12**, 305–314 (2002).
66. Kampa, B. M., Letzkus, J. J. & Stuart, G. J. Requirement of dendritic calcium spikes for induction of spike-timing-dependent synaptic plasticity. *J. Physiol.* **574**, 283–290 (2006).
67. Artola, A., Bröcher, S. & Singer, W. Different voltage-dependent thresholds for inducing long-term depression and long-term potentiation in slices of rat visual cortex. *Nature* **347**, 69–72 (1990).
68. Malenka, R. C. & Bear, M. F. LTP and LTD: An embarrassment of riches. *Neuron* **44**, 5–21 (2004).
69. Kampa, B. M., Clements, J., Jonas, P. & Stuart, G. J. Kinetics of Mg2+ unblock of NMDA receptors: implications for spike-timing dependent synaptic plasticity. *J. Physiol.* **556**, 337–345 (2004).
70. Froemke, R. C., Poo, M. M. & Dan, Y. Spike-timing-dependent synaptic plasticity depends on dendritic location. *Nature* **434**, 221–225 (2005).
71. Bender, V. A., Bender, K. J., Brasier, D. J. & Feldman, D. E. Two coincidence detectors for spike timing-dependent plasticity in somatosensory cortex. *J. Neurosci.* **26**, 4166–4177 (2006).
72. Banerjee, A. et al. Double dissociation of spike timing-dependent potentiation and depression by subunit-preferring NMDA receptor antagonists in mouse barrel cortex. *Cereb. Cortex* **19**, 2959–2969 (2009).
73. Inglebert, Y., Aljadeff, J., Brunel, N. & Debanne, D. Synaptic plasticity rules with physiological calcium levels. *Proc. Natl. Acad. Sci.* **117**, 33639–33648 (2020).
74. Gómez, R. et al. NMDA receptor-BK channel coupling regulates synaptic plasticity in the barrel cortex. *Proc. Natl. Acad. Sci.* **118**, e2107026118 (2021).
75. Kumar, A., Barkai, E. & Schiller, J. Plasticity of olfactory bulb inputs mediated by dendritic nmda-spikes in rodent piriform cortex. *eLife* **10**, e70383 (2021).
76. Wigstrom, H. & Gustafsson, B. Postsynaptic control of hippocampal long-term potentiation. *J. Physiol.* **81**, 228–236 (1986).
77. Lisman, J. A mechanism for the Hebb and the anti-Hebb processes underlying learning and memory. *Proc. Natl. Acad. Sci.* **86**, 9574–9578 (1989).
78. Pouille, F. & Scanziani, M. Enforcement of temporal fidelity in pyramidal cells by somatic feed-forward inhibition. *Science* **293**, 1159–1163 (2001).
79. Higley, M. J. & Contreras, D. Balanced excitation and inhibition determine spike timing during frequency adaptation. *J. Neurosci.* **26**, 448–457 (2006).
80. Fino, E. et al. Distinct coincidence detectors govern the corticostriatal spike timing-dependent plasticity. *J. Physiol.* **588**, 3045–3062 (2010).
81. Paille, V. et al. GABAergic circuits control spike-timing-dependent plasticity. *J. Neurosci.* **33**, 9353–9363 (2013).
82. Dahmen, J. C., Hartley, D. E. H. & King, A. J. Stimulus-timing-dependent plasticity of cortical frequency representation. *J. Neurosci.* **28**, 13629–13639 (2008).
83. Zucker, R. S. & Regehr, W. G. Short-term synaptic plasticity. *Ann. Rev. Physiol.* **64**, 355–405 (2002).
84. Malinow, R. & Tsien, R. W. Presynaptic enhancement shown by whole-cell recordings of long-term potentiation in hippocampal slices. *Nature* **346**, 177–180 (1990).
85. Manabe, T., Wyllie, D. J. A., Perkel, D. J. & Nicoll, R. A. Modulation of synaptic transmission and long-term potentiation: effects on paired pulse facilitation and EPSC variance in the CA1 region of the hippocampus. *J. Neurophysiol.* **70**, 1451–1459 (1993).
86. Brock, J. A., Thomazeau, A., Watanabe, A., Li, S. S. Y. & Sjöström, P. J. A practical guide to using CV analysis for determining the locus of synaptic plasticity. *Front. Syn. Neurosci.* **12**, 11 (2020).
87. McLachian, E. M. The statistics of transmitter release at chemical synapses. *Int. Rev. Physiol.* **17**, 49–117 (1978).
88. Bekkers, J. M., Richerson, G. B. & Stevens, C. F. Origin of variability in quantal size in cultured hippocampal neurons and hippocampal slices. *Proc. Natl. Acad. Sci.* **87**, 5359 (1990).
89. Markram, H., Lübke, J., Frotscher, M. & Sakmann, B. Regulation of synaptic efficacy by coincidence of postsynaptic APs and EPSPs. *Science* **275**, 213–215 (1997).
90. Debanne, D., Gähwiler, B. H. & Thompson, S. M. Long-term synaptic plasticity between pairs of individual CA3 pyramidal cells in rat hippocampal slice cultures. *J. Physiol.* **507**, 237–247 (1998).
91. Nishiyama, M., Hong, K., Mikoshiba, K., Poo, M. M. & Kato, K. Calcium stores regulate the polarity and input specificity of synaptic modification. *Nature* **408**, 584–588 (2000).
92. Sjöström, P. J., Turrigiano, G. G. & Nelson, S. B. Rate, timing, and cooperativity jointly determine cortical synaptic plasticity. *Neuron* **32**, 1149–1164 (2001).
93. Fino, E., Glowinski, J. & Venance, L. Bidirectional activity-dependent plasticity at corticostriatal synapses. *J. Neurosci.* **25**, 11279–11287 (2005).
94. Wittenberg, G. M. & Wang, S. S. H. Malleability of spike-timing-dependent plasticity at the CA3-CA1 synapse. *J. Neurosci.* **26**, 6610–6617 (2006).
95. Buchanan, K. A. & Mellor, J. R. The activity requirements for spike timing-dependent plasticity in the hippocampus. *Front. Syn. Neurosci.* **2**, 11 (2010).
96. Larsen, R. S., Rao, D., Manis, P. B. & Philpot, B. D. STDP in the developing sensory neocortex. *Front. Syn. Neurosci.* **2**, 9 (2010).
97. Bell, C. C., Han, V. Z., Sugawara, Y. & Grant, K. Synaptic plasticity in a cerebellum-like structure depends on temporal order. *Nature* **387**, 278–281 (1997).
98. Han, V. Z., Grant, K. & Bell, C. C. Reversible associative depression and nonassociative potentiation at a parallel fiber synapse. *Neuron* **27**, 611–622 (2000).

99. Piochon, C., Kruskal, P., Maclean, J. & Hansel, C. Non-Hebbian spike-timing-dependent plasticity in cerebellar circuits. *Front. Neural Circuits* **6**, 124 (2012).
100. Sjöström, P. J. & Häusser, M. A cooperative switch determines the sign of synaptic plasticity in distal dendrites of neocortical pyramidal neurons. *Neuron* **51**, 227–238 (2006).
101. Kampa, B. M., Letzkus, J. J. & Stuart, G. J. Dendritic mechanisms controlling spike-timing-dependent synaptic plasticity. *Trends Neurosci*. **30**, 456–463 (2007).
102. Ascher, P., Dieudonne, S., MacDonald, J. & Sather, W. Kinetics of activation, deactivation and desensitization of the ''NMDA'' glutamate receptor. In *Comptes Rendus de l'Academie des Sciences - Serie III* vol. 314 (CRC Press/Taylor and Francis, 1992).
103. D'Angelo, E., Rossi, P. & Taglietti, V. Voltage-dependent Kinetics of N-Methyl-d-aspartate synaptic currents in rat cerebellar granule cells. *Eur. J. Neurosci.* **6**, 640–645 (1994).
104. Karmarkar, U. R. & Buonomano, D. V. A model of spike-timing dependent plasticity: One or two coincidence detectors? *J. Neurophysiol.* **88**, 507–513 (2002).
105. Dugué, G. P. et al. Electrical coupling mediates tunable low-frequency oscillations and resonance in the cerebellar golgi cell network. *Neuron* **61**, 126–139 (2009).
106. Gurnani, H. & Silver, R. A. Multidimensional population activity in an electrically coupled inhibitory circuit in the cerebellar cortex. *Neuron* **109**, 1739–1753 (2021).
107. Vervaeke, K. et al. Rapid desynchronization of an electrically coupled interneuron network with sparse excitatory synaptic input. *Neuron* **67**, 435–451 (2010).
108. van Welie, I., Roth, A., Ho, S. S. N., Komai, S. & Häusser, M. Conditional spike transmission mediated by electrical coupling ensures millisecond precision-correlated activity among interneurons in Vivo. *Neuron* **90**, 810–823 (2016).
109. Garrido, J. A., Ros, E. & D'Angelo, E. Spike timing regulation on the millisecond scale by distributed synaptic plasticity at the cerebellum input stage: a simulation study. *Front. Comput. Neurosci.* **7**, 64 (2013).
110. Wehr, M. & Zador, A. M. Balanced inhibition underlies tuning and sharpens spike timing in auditory cortex. *Nature* **426**, 442–446 (2003).
111. Tepper, J. M., Wilson, C. J. & Koós, T. Feedforward and feedback inhibition in neostriatal GABAergic spiny neurons. *Brain Res. Rev.* **58**, 272–281 (2008).
112. Pawlak, V. & Kerr, J. N. D. Dopamine receptor activation is required for corticostriatal spike-timing-dependent plasticity. *J. Neurosci.* **28**, 2435–2446 (2008).
113. Shen, W., Flajolet, M., Greengard, P. & Surmeier, D. J. Dichotomous dopaminergic control of striatal synaptic plasticity. *Science* **321**, 848–851 (2008).
114. Pellerin, J. P. & Lamarre, Y. Local field potential oscillations in primate cerebellar cortex during voluntary movement. *J. Neurophysiol.* **78**, 3502–3507 (1997).
115. Hartmann, M. J. & Bower, J. M. Oscillatory activity in the cerebellar hemispheres of unrestrained rats. *J. Neurophysiol.* **80**, 1598–1604 (1998).
116. Cheron, G., Márquez-Ruiz, J. & Dan, B. Oscillations, Timing, Plasticity, and Learning in the Cerebellum. *Cerebellum* **15**, 122–138 (2016).
117. Parker, K. L. Timing tasks synchronize cerebellar and frontal ramping activity and theta oscillations: implications for cerebellar stimulation in diseases of impaired cognition. *Front. Psychiatry* **6**, 190 (2016).
118. Courtemanche, R., Robinson, J. C. & Aponte, D. I. Linking oscillations in cerebellar circuits. *Front. Neural Circuits* **7**, 125 (2013).
119. Courtemanche, R. & Lamarre, Y. Local field potential oscillations in primate cerebellar cortex: synchronization with cerebral cortex during active and passive expectancy. *J. Neurophysiol.* **93**, 2039–2052 (2005).
120. Frederick, A., Bourget-Murray, J., Andrew Chapman, C., Amir, S. & Courtemanche, R. Diurnal influences on electrophysiological oscillations and coupling in the dorsal striatum and cerebellar cortex of the anesthetized rat. *Front. Syst. Neurosci.* **8**, 145 (2014).
121. Luque, N. R. et al. Distributed cerebellar motor learning: a spike-timing-dependent plasticity model. *Front. Comput. Neurosci.* **10**, 17 (2016).
122. Egger, V., Feldmeyer, D. & Sakmann, B. Coincidence detection and changes of synaptic efficacy in spiny stellate neurons in rat barrel cortex. *Nat. Neurosci.* **2**, 1098–1105 (1999).
123. Wang, Y. T. & Linden, D. J. Expression of cerebellar long-term depression requires postsynaptic clathrin-mediated endocytosis. *Neuron* **25**, 635–647 (2000).
124. Sjöström, P. J., Turrigiano, G. G. & Nelson, S. B. Neocortical LTD via coincident activation of presynaptic NMDA and cannabinoid receptors. *Neuron* **39**, 641–654 (2003).
125. Banerjee, S., Riordan, M. & Bhat, M. A. Genetic aspects of autism spectrum disorders: Insights from animal models. *Front. Cell. Neurosci.* **8**, 58 (2014).
126. Yang, Y. & Calakos, N. Presynaptic long-term plasticity. *Front. Syn. Neurosci.* **5**, 8 (2013).
127. Faber, D. S., Korn, H. & Lin, J. W. Role of medullary networks and postsynaptic membrane properties in regulating mauthner cell responsiveness to sensory excitation. *Brain Behav. Evol.* **37**, 286–297 (1991).
128. Schulz, P. E., Cook, E. P. & Johnston, D. Changes in paired-pulse facilitation suggest presynaptic involvement in long-term potentiation. *J. Neurosci.* **14**, 5325–5337 (1994).
129. Saviane, C. & Silver, R. A. Fast vesicle reloading and a large pool sustain high bandwidth transmission at a central synapse. *Nature* **439**, 983–987 (2006).
130. Loebel, A. et al. Multiquantal release underlies the distribution of synaptic efficacies in the neocortex. *Front. Comput. Neurosci.* **3**, 27 (2009).
131. Mizusaki, B. E. P., Li, S. S. Y., Costa, R. P. & Sjöström, P. J. Pre- and postsynaptically expressed spike-timing-dependent plasticity contribute differentially to neuronal learning. *PLoS Comput. Biol.* **18**, e1009409 (2022).
132. Nieus, T. et al. LTP regulates burst initiation and frequency at mossy fiber-granule cell synapses of rat cerebellum: experimental observations and theoretical predictions. *J. Neurophysiol.* **95**, 686–699 (2006).
133. Costa, R. P., Froemke, R. C., Sjöström, P. J. & van Rossum, M. C. W. Unified pre- and postsynaptic long-term plasticity enables reliable and flexible learning. *Elife* **4**, e09457 (2015).
134. Blackman, A. V., Abrahamsson, T., Costa, R. P., Lalanne, T. & Sjöström, P. J. Target-cell-specific short-term plasticity in local circuits. *Front. Syn. Neurosci.* **5**, 11 (2013).
135. Mapelli, L., Pagani, M., Garrido, J. A. & D'Angelo, E. Integrated plasticity at inhibitory and excitatory synapses in the cerebellar circuit. *Front. Cell Neurosci.* **9**, 169 (2015).
136. Dean, P., Porrill, J., Ekerot, C. & Neuroscience, H. J.-N. R. The cerebellar microcircuit as an adaptive filter: experimental and computational evidence. *Nat. Rev. Neurosci.* **11**, 30–43 (2009).


## Acknowledgements

This project/research is supported by #NEXTGENERATIONEU (NGEU) and funded by the Ministry of University and Research (MUR), National Recovery and Resilience Plan (NRRP), project MNESYS (PE0000006)—A Multiscale integrated approach to the study of the nervous system in health and disease (DN. 1553 11.10.2022) to E.D. and E.P., and by EBRAINS-Italy (IR00011) Project IR11– EBRAINS-Italy - M4C2 Line 3.1 of the PNRR, Action 3.1.1 – Funded by European Commission—NextGenerationEU (CUP

B51E22000150006) to S.M. The authors gratefully acknowledge the Centro Grandi Strumenti, the Confocal Microscopy Facility, particularly A.O. and P.V. for their invaluable support and assistance in this work.

## Author contributions

E.P. performed electrophysiological experiments, analyzed the data, and created all the illustrations; S.M. designed the models and performed the simulations; D.D.D. performed the morphological reconstructions; T.S. established the STDP induction protocol; E.P., F.P., and E.D. contributed to paper writing and revision; F.P. and E.D. coordinated research and wrote the final version of the paper.

## Competing interests

The authors declare no competing interests.

## Additional information

**Supplementary information** The online version contains supplementary material available at https://doi.org/10.1038/s42003-025-08153-1.

**Correspondence** and requests for materials should be addressed to Francesca Prestori or Egidio D'Angelo.

**Peer review information** *Communications Biology* thanks the anonymous reviewers for their contribution to the peer review of this work. Primary Handling Editor: B.B. A peer review file is available.